Spring 5-15-2020

# Experimental Reduction Of Fe-Oxyhydroxides In Simulated Carbonate and Sulfide/Sulfate Brine: Implications for Paleolake Deposits.

Joshua M. Chidzugwe
*Georgia State University*

# EXPERIMENTAL REDUCTION OF FE-OXYHYDROXIDES IN SIMULATED CARBONATE AND SULFIDE/SULFATE BRINE: IMPLICATIONS FOR PALEOLAKE DEPOSITS

By

JOSHUA CHIDZUGWE

Under the Direction of Daniel M. Deocampo, Ph.D.

## ABSTRACT

Mineral reduction simulations imitating various geochemical environments were conducted over 1 – 30 hours. Ferrihydrite was prepared from solid phases using a solvent-deficient method. In each experiment, ferrihydrite was abiotically reduced with sodium dithionite solution in 1 Molar buffered Na-carbonate and Na-sulfate/sulfide brine at 70°C under nitrogen atmosphere. Six (n=6) and ten (n=10) samples of resultant sulfate/sulfide and carbonate precipitates were collected, respectively. X-Ray Diffractometry (XRD) and Scanning Electron Microscopy (SEM) analytical methods were used to characterize the experimental products. Diagenetic siderite and goethite in carbonate simulations were identified with XRD. Siderite was observed as spherules and platy structures possibly of chukanovite. Calculations using PHREEQ software predicted siderite and pyrite forming in carbonate and sulfate/sulfide brines respectively. The expected pyrite did not precipitate. Rather magnetite, which was unexpected, was formed by either partial reduction of ferrihydrite or partial oxidation of an intermediate reduced phase such as wüstite. Understanding the diagenetic pathways and water-mineral interactions of these systems is necessary for paleoenvironmental reconstruction and for the fidelity of paleomagnetic records.

INDEX WORDS: Ferrihydrite, Diagenesis, Reduction, Siderite, Magnetite.

# EXPERIMENTAL REDUCTION OF FE-OXYHYDROXIDES IN SIMULATED CARBONATE AND SULFIDE/SULFATE BRINE: IMPLICATIONS FOR PALEOLAKE DEPOSITS

by

JOSHUA CHIDZUGWE

A Thesis Submitted in Partial Fulfillment of the Requirements for the Degree of

Master of Science

in the College of Arts and Sciences

Georgia State University

2019

# EXPERIMENTAL REDUCTION OF FE-OXYHYDROXIDES IN SIMULATED CARBONATE AND SULFIDE/SULFATE BRINE: IMPLICATIONS FOR PALEOLAKE DEPOSITS.

by

JOSHUA CHIDZUGWE

Committee Chair: Daniel M. Deocampo

Committee: Nadine S. Kabengi

W. Crawford Elliott

Electronic Version Approved:

Office of Graduate Studies

College of Arts and Sciences

Georgia State University

December 2019

## DEDICATION

I would like to dedicate this report to my dear wife, Carolyn Akol, my treasured son, Ethan M. Malidzo and last but not least my parents, Mr. John M. Malidzo C. and Mrs. Judith Malidzo C. the great people who raised me to be the man I stand to be this day and my brother, Samson M. Chidzugwe.

To Ethan, may you achieve greater things than your old man.

## ACKNOWLEDGEMENTS

I must thank a cast of many for their indirect and direct contributions to the notions and efforts that have borne fruit to the writing of this thesis. It is not in order to cite them all here, but for those not mentioned an apology is in order.

Firstly, I pass my earnest gratitude to the Almighty God for the unreserved mercies, grace and love He offered for the completion of this thesis.

Secondly, I would like to appreciate the NSF funding 1029020, 1349599 and ACS/PRF funding 58131-UR2 and pass my appreciation to my supervisor, Prof. Daniel Deocampo and my thesis committee members, Prof. Nadine Kabengi and Prof. Crawford Elliott, for the patience and guidance through the fulfilment of this thesis. I appreciate the assistance and lessons taught all through. I'm truly humbled by the guidance offered.

To Prof. K. Hankins, Chair of Geosciences department; Prof. L. Kiage, Associate Professor of Geosciences; Prof. B. Meyer, Environmental Geology Lecturer; Prof. C. Visaggi, Teaching Practicum Lecturer, J. Kirn and B. Lawal, I pass my indebtedness for the advice and support along my journey through graduate school. To Dr. D. Gebregiorgis, thank you for the pieces of advice you have always given me on academia and life generally. To Dr. N. Rabideaux, Rutgers University, thank you for helping with the SEM analysis.

Lastly, heartfelt thanks to my family and friends, Christa Koki, Lucas Mwasya, Jacob Jok, David Davis, Marcos Gamboa, Benjamin Opiyo, Vicky Chelang'at and colleagues in general. Thank you for all the efforts and support in the quest for helping and encouraging me during the writing of this thesis, you encouraged me in one way or the other.

And to all the great people who came into my life, thank you for the lessons you taught me along. The list is too long to exhaust, though I give much sincere gratitude to each and every individual who helped me in my growth. Any omissions in this acknowledgement does not show lack of appreciation. May God bless this great nation, America.

**TABLE OF CONTENTS**

# LIST OF TABLES

## LIST OF FIGURES

# LIST OF ABBREVIATIONS

HSPDP – Hominin Sites and Paleolakes Drilling Project

XRD – X-Ray Diffractometer

SEM – Scanning Electron Microscope

nm – Nanometers

# 1 INTRODUCTION

Understanding the elemental distribution in lake sedimentary environments is notably linked to external climatic conditions, which influence the precipitation of particular mineral phases (Cohen, 2003). Generally, geochemical environments in sediments and sedimentary rocks are categorized based on their hydrogen ion activity and redox potentials. (Berner, 1981; Fernandez et al., 2014).

The primary source of iron in lacustrine settings is typically from stream load complexed by organic matter suspended in sediments at the sediment-water interface, where stable iron (III) converts to mobile reactive iron (II). Iron reduction in anoxic conditions increases with depth, thereby increasing the concentration of iron (II) in pore waters. (Berner, 1981; Pye et al., 1990; Nodder et al., 2005).

The Hominin Sites and Paleolakes Drilling Project (HSPDP) is responsible for correlating the history of hominin evolution with regional climatic variations. The project collected over 2 kilometers of lake sediment cores from six basins near-critical archeological sites along the eastern branch of the East African Rift Valley (Figure 1-4). HSPDP's objective is building a high resolution regional framework of climatic and habitual changes during the hominin evolution (Campisano et al., 2017).

Stratigraphic correlations of the upper-middle drill core sections of the NAO14-1B and NAW14-1A indicated the presence of gypsum ($CaSO_4{\cdot}2H_2O$) and pyrite ($Fe_2S$) in varying amounts suggesting sub-lacustrine sulfate reduction (Figure 1-1). The NAO core contained abundant gypsum and almost no pyrite, indicating that NAO sediment was shallower hence undergoing greater oxidation compared to sediments in the NAW core. These minerals are potential terrestrial paleoenvironmental redox proxies in understanding the redox conditions for the paleo-lakes paleo-bathymetry (Davis et al., 2017). Based on the drill core section NAW of the HSPDP, pyrite forms at the geological contacts of basalt. The formation of the pyrite

possibly attributed to the interaction of basalt and aqueous dissolved $H_2S$-CO in the surrounding geological environment.

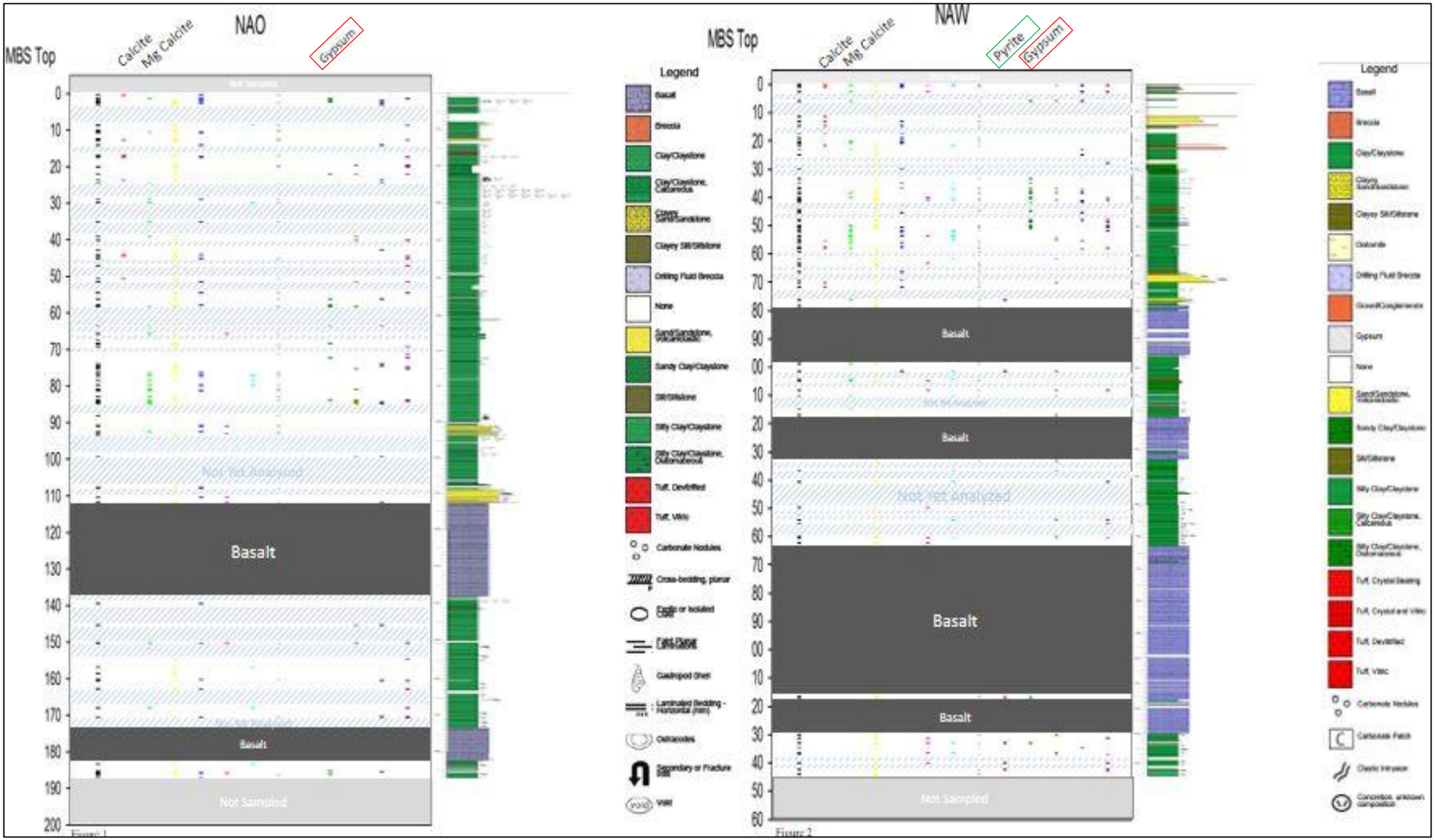


*Figure 1-1. Mineralogical plots of NAO and NAW drill core sections from HSPDP. (Davis et al., 2017)*

Siderite formation involves iron reduction and bacterial methanogenesis of organic carbon compounds (see Equation 1-1 below). Siderite is known to form in non-marine environments. In marine environments, it is difficult to precipitate siderite because readily available $Ca^{2+}$ preferentially reacts with present bicarbonate at normal marine temperatures. Eodiagenetic siderite is noted as a reducing environment proxy in sedimentary environments (Bennington, 1999; Pye, 1984; Rodrigues et al., 2015).

$$7CH_2O + 2Fe_2O_3 \rightarrow 3CH_4 + 4FeCO_3 + H_2O \ldots \text{(Eqn. 1-1; Curtis, 1986)}$$

Pyrite is documented to form when detrital (III) iron oxide (see Equation 1-2 below) or elemental iron reacts with $H_2S_{(g)}$ during early diagenesis in anoxic conditions. During this reaction, metastable forms of iron mono-sulfides form before the final product, pyrite. In natural sedimentary environments, $H_2S_{(g)}$ is derived from sulfate reduction in interstitial pore-waters by existing bacterial agents (See Figure 1-2). For the case of our simulation experiment, the sodium dithionite acts as the reducing agent for Fe. The anoxic environment was created by purging the apparatus with nitrogen gas.

$$S_0 + Fe_2O_3 + 3H_2S \rightarrow 2FeS_2 + 3H_2O \ldots \text{(Eqn. 1-2; Berner, 1981)}$$

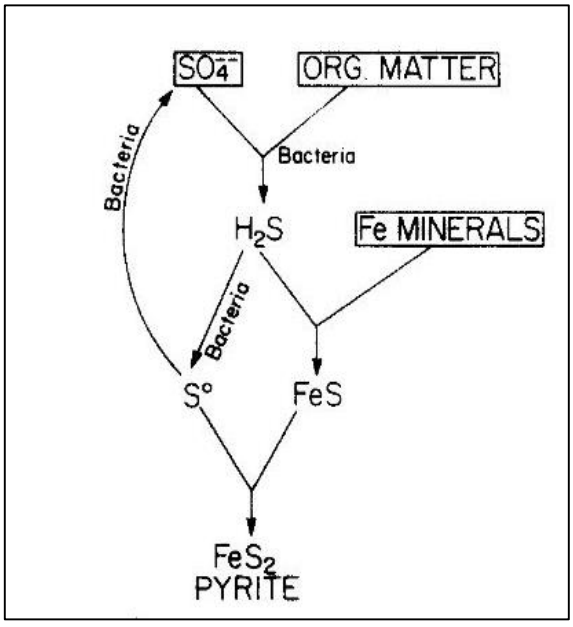


*Figure 1-2. Diagrammatic representation of the general process of sedimentary pyrite formation (Berner, 1984).*

Similarly, to siderite, pyrite is formed in reducing, sulfidic conditions associated with carbonaceous material and may be deposited in lacustrine muds by the action of microorganisms (Phillips and Griffen, 1981). The development of siderite and pyrite requires anoxic sedimentary environments in the presence of $Fe^{2+}$, both forming with increasing organic matter and low sediment supply regimes (Hlal, 2013). When exposed to oxidizing environments, they are both oxidized to goethite or hematite.

Ferrihydrite is omnipresent in sediments, and because of its reactivity and high ion adsorption capacity, it serves as the primary sink for different metals (Hansel et al., 2005). Iron Eh-pH diagrams best demonstrate the solubility fields of the dissolved and solid species of iron (See Figures 1-3 and 1-4). Siderite and pyrite as our minerals of interest to lie within the reduction zone in the Eh-pH diagram.

Redox reactions are considered significant in the determination of the distribution of minor elements in closed basins (Deocampo and Jones, 2014). Hence, comprehending the formation and timing of siderite and pyrite through laboratory simulations will give a sensible explanation of significant reduction conditions during diagenesis in lacustrine basins. Besides, siderite is useful in paleoenvironmental studies because of its close association with pore-water chemistry without necessarily undergoing recrystallization (Mozley, 1989; Lim et al., 2004). Lake Bogoria and Aral sea are relevant case studies due to the high ionic carbonate and sulfate concentrations (see Table 1-1), respectively (Deocampo and Jones, 2014).

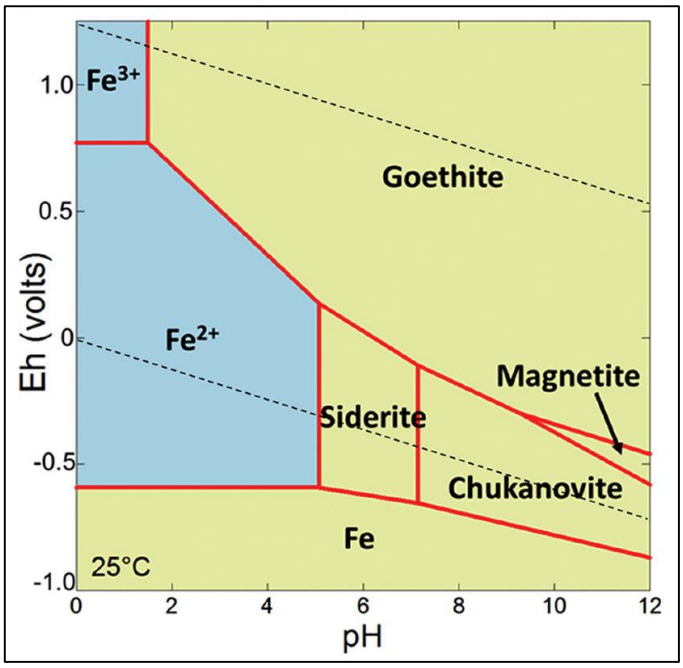


*Figure 1-3. Eh-pH diagram for Iron showing solubility fields of solid species and dissolved species at 25°C (Russell et al., 2010)*

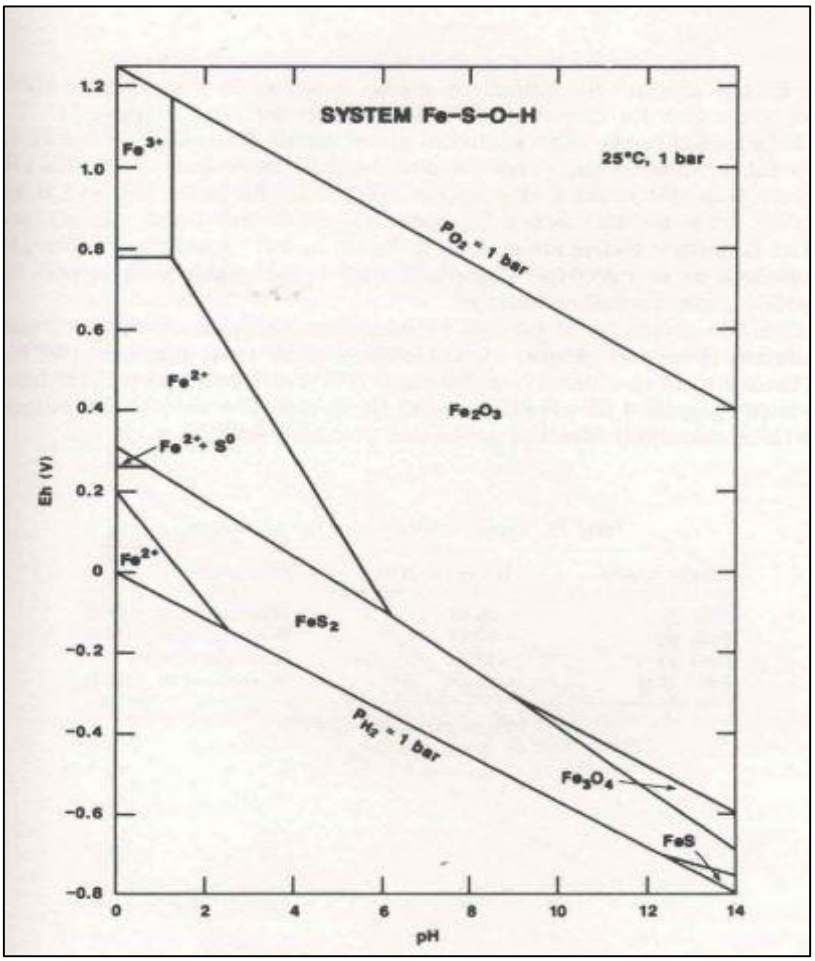


*Figure 1-4. Eh-pH diagram for Iron-Sulfur-Oxygen-Hydrogen showing solubility fields of solid species and dissolved species at 25°C (Brookins., 2012)*

## 1.1 Case Studies.

### *1.1.1 Lake Bogoria*

Widely known for its flamingo populations and various bird species Lake Bogoria is an alkaline, perennial closed – basin lake formed through tectonic activity. The lake is located approximately 55 km north of the Menegai Volcano within the East African Rift Valley in the Gregory Rift (Figure 1-4). Active volcanism within the rift has played a major role in the hydrological and morphological features of lake basins within it, with major differences displayed in the dissolved salt concentrations (Schlueter, 1997). Bogoria has a small surface to volume ratio displaying highly alkaline salinity levels of > 40% with $Na^+ > K^+ > Si^{4+} > Ca^{2+}$ and $HCO_3^- > CO_3^{2-} > Cl^- > F^- > SO_4^{2-}$. The high ionic concentrations of these constituents are eminent due to the erosion of the alkaline volcanic rocks found in the Rift valley (Deocampo and Jones, 2003; Scoon, 2018). Hydrothermal springs, geysers, ephemeral tributaries, and surface runoff from surrounding highlands feed the lake (Jirsa et al., 2013). Evaporative concentration and binary mixing of river and thermal waters explain the chemical composition of the lake waters (Tarits et al., 2006)

### *1.1.2 Aral Sea*

Located in Central Asia, the Aral Sea is considered a terminal lake that lies in the Kara-Kum and Kyzyl-Kum region, bordering Kazakhstan, Turkmenistan, and Uzbekistan (see Figure 1-5). The lake is situated in an arid/semi-arid climatic environment and theorized to have formed through continued deflation processes through wind erosion. Over the past years, drastic changes in the water level and chemistry have been observed due to excessive irrigation from the in-flowing rivers causing increased salinity levels (Boomer et al., 2000; Boomer, 1993). Global warming is a significant "future" contributor to the decreased water level changes due to excessive evaporation (Micklin, 2010). The two main tributaries, namely the *Amu Darya* and the *Syr Darya*, flow into the lake to the South and East, respectively. Low concentrations of $Cl^-$ and $HCO_3^-$ ions with relatively high levels of $Mg^{2+}$ and $SO_4^{2-}$ ions were observed through chemical analysis of the evaporitic sediments in the lake. $SO_4^{2-}$ evaporite

deposits in the basin are the notable species as a result of the chemistry of the in-flowing river water.

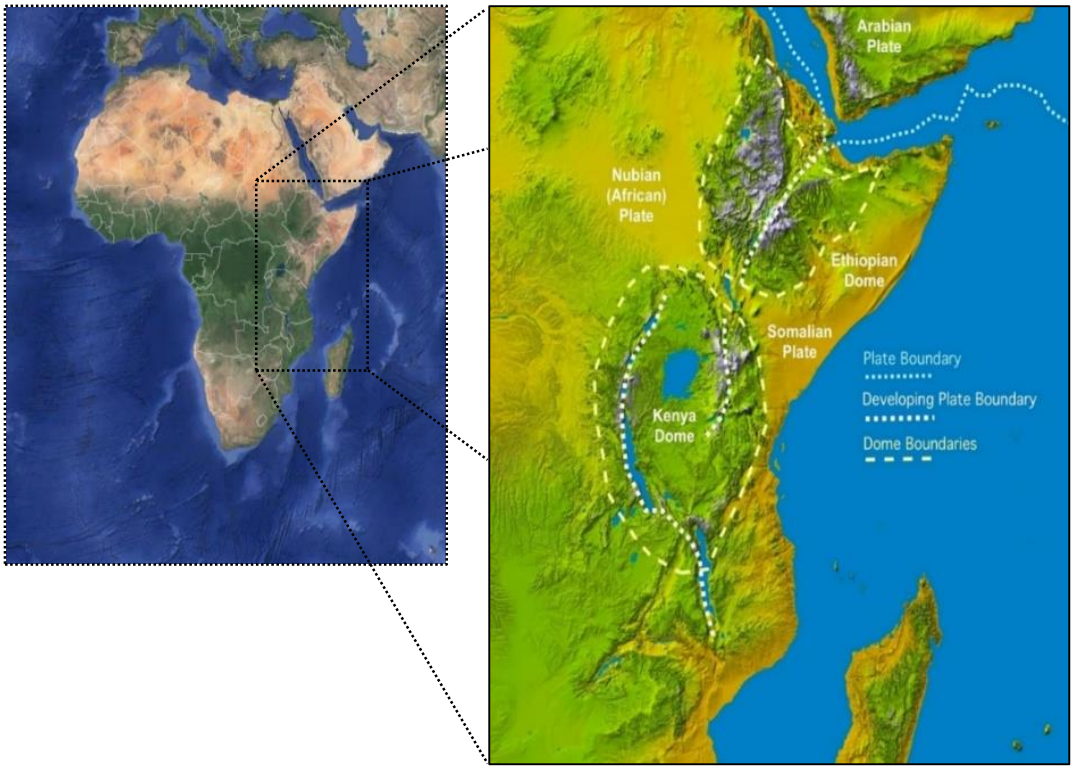


*Figure 1-5. The Great East African Rift valley (Wood and Guth, 2013).*


*Figure 1-6 Geographic location of Aral Sea. Time image was taken Aral Sea had dried up into two separate basins (Google Earth, 2020).*

*Table 1-1. Cation-Anion associations in mol% (Deocampo and Jones, 2014)*

| Locality | $Na_2Cl_2$ | $K_2Cl_2$ | $CaCl_2$ | $MgCl_2$ | $Na_2SO_4$ | $K_2SO_4$ | $CaSO_4$ | $MgSO_4$ | $Na_2CO_3$ | $CaCO_3$ | $MgCO_3$ |
|---|---|---|---|---|---|---|---|---|---|---|---|
| Western Asia | (Blinov, 1962; Clauer et al., 1998; Kosarev and Yablonskaya, 1994) | | | | | | | | | | |
| Aral Sea | 59.0 | 0.19 | 0.0 | 0.4 | 0.0 | 0.58 | 12.7 | 25.4 | 0.0 | 0.0 | 1.7 |
| Lake Balkhash (delta) | 33.7 | 0.0 | 0.0 | 0.0 | 22.8 | 0.0 | 13.8 | 2.1 | 0.0 | 0.0 | 27.6 |
| Lake Balkhash (center) | 38.4 | 0.0 | 0.0 | 0.0 | 32.3 | 0.0 | 0.8 | 10.0 | 0.0 | 0.0 | 18.4 |
| Caspian Sea | 62.4 | 1.1 | 0.0 | 5.7 | 0.0 | 0.0 | 8.5 | 20.3 | 0.0 | 0.0 | 2.0 |
| Caspian Sea tributaries | 12.5 | 0.0 | 0.0 | 0.0 | 7.3 | 0.6 | 51.4 | 6.5 | 0.0 | 0.0 | 21.6 |
| Caspian Sea hot springs | 58.0 | 1.9 | 0.2 | 7.9 | 0.0 | 0.0 | 32.0 | 0.0 | 0.0 | 0.0 | 0.0 |
| Qaidam Basin, China | (Spencer et al., 1990; Zheng, 1997) | | | | | | | | | | |
| Nyer Co | 15.0 | 6.5 | 0.0 | 74.0 | 0.0 | 0.0 | 0.6 | 3.8 | 0.0 | 0.0 | 0.0 |
| Qinghai | 54.3 | 10.9 | 0.0 | 2.7 | 0.0 | 0.4 | 0.8 | 30.9 | 0.0 | 0.0 | 0.0 |
| GSL Basin, USA | (Spencer et al., 1985a; Kohler, 2002; USGS, 2002) | | | | | | | | | | |
| Salt Lake | 83.7 | 2.4 | 0.0 | 5.9 | 0.0 | 0.0 | 0.3 | 7.7 | 0.0 | 0.0 | 0.1 |
| Bear River | 44.3 | 0.0 | 0.0 | 0.0 | 0.1 | 2.4 | 6.1 | 0.0 | 0.0 | 23.3 | 23.8 |
| Sevier River | 49.5 | 0.0 | 0.0 | 0.0 | 11.2 | 0.7 | 12.9 | 8.1 | 0.0 | 0.0 | 17.6 |
| Malad Springs | 89.0 | 2.8 | 3.3 | 2.6 | 0.0 | 0.0 | 1.3 | 0.0 | 0.0 | 1.0 | 0.0 |
| West Pond | 87.6 | 3.4 | 0.9 | 6.2 | 0.0 | 0.0 | 2.0 | 0.0 | 0.0 | 0.0 | 0.0 |
| Lake Bogoria Basin, Kenya | (Renaut and Tiercelin, 1994) | | | | | | | | | | |
| Lake Bogoria | 14.4 | 0.5 | 0.0 | 0.0 | 0.2 | 0.5 | 0.0 | 0.0 | 84.0 | 0.1 | 0.0 |
| Sandai River | 22.0 | 0.7 | 0.0 | 0.0 | 0.5 | 1.4 | 0.0 | 0.0 | 41.0 | 24.6 | 9.8 |
| Loburu hot spring | 11.8 | 0.0 | 0.0 | 0.0 | 1.1 | 1.1 | 0.0 | 0.0 | 85.8 | 0.1 | 0.1 |
| Northern Great Plains, USA and Canada | (Komor, 1994; Last, 1994a; USGS, 2002) | | | | | | | | | | |
| Big Coulee Riv. | 3.2 | 0.0 | 0.0 | 0.0 | 9.8 | 2.4 | 0.0 | 0.0 | 0.1 | 52.5 | 32.1 |
| Souris River | 8.8 | 0.0 | 0.0 | 0.0 | 28.0 | 3.5 | 0.0 | 0.0 | 6.5 | 22.1 | 31.2 |
| Sheyenne River | 5.1 | 0.0 | 0.0 | 0.0 | 25.9 | 0.0 | 0.0 | 0.0 | 24.0 | 18.8 | 26.2 |
| Des Lacs River | 5.8 | 0.0 | 0.0 | 0.0 | 9.3 | 17.3 | 0.2 | 0.0 | 0.0 | 42.1 | 25.3 |
| Little Manitou Lake | 22.9 | 0.0 | 0.0 | 0.0 | 1.7 | 1.0 | 2.3 | 71.2 | 0.0 | 0.0 | 0.9 |
| Freefight Lake | 12.5 | 0.0 | 0.0 | 0.0 | 29.8 | 3.5 | 0.5 | 50.5 | 0.0 | 0.0 | 3.2 |
| Devils Lake | 20.7 | 0.0 | 0.0 | 0.0 | 40.3 | 4.5 | 5.7 | 19.1 | 0.0 | 0.0 | 9.7 |
| Death Valley, USA | (Li et al., 1997) | | | | | | | | | | |
| Amargosa River | 57.2 | 0.0 | 0.0 | 0.0 | 31.5 | 2.6 | 0.0 | 0.0 | 2.1 | 3.4 | 3.2 |
| Mormon Point Springs | 79.8 | 2.8 | 8.3 | 5.6 | 0.0 | 0.0 | 3.4 | 0.0 | 0.0 | 0.1 | 0.0 |
| DV-40 | 97.4 | 0.0 | 0.0 | 0.0 | 0.0 | 0.7 | 1.2 | 0.6 | 0.0 | 0.0 | 0.0 |
| Australia | (Herczeg and Lyons, 1991; Johnson, 1980; Mann, 1983) | | | | | | | | | | |
| Yilgarn | 78.9 | 0.7 | 0.0 | 12.6 | 0.0 | 0.0 | 3.5 | 4.3 | 0.0 | 0.0 | 0.0 |
| Lake Tyrrell | 82.8 | 0.7 | 0.0 | 8.0 | 0.0 | 0.0 | 0.3 | 8.2 | 0.0 | 0.0 | 0.0 |
| Lake Eyre | 87.6 | 0.7 | 0.0 | 5.0 | 0.0 | 0.0 | 0.6 | 6.0 | 0.0 | 0.0 | 0.1 |
| Dead Sea basin | (Neev and Emery, 1967; Abed et al., 1990; Vengosh and Rosenthal, 1994) | | | | | | | | | | |
| Jordan River | 39.3 | 4.7 | 0.0 | 1.5 | 0.0 | 0.0 | 4.2 | 0.0 | 0.0 | 21.8 | 29.8 |
| Zohar Springs | 26.4 | 2.8 | 16.8 | 49.7 | 0.0 | 0.0 | 1.2 | 0.0 | 0.0 | 0.03 | 0.03 |
| Dead Sea | 28.1 | 2.7 | 14.2 | 54.6 | 0.0 | 0.0 | 0.3 | 0.0 | 0.0 | 0.04 | 0.04 |
| Other Great Basin, USA | (Rosen, 1991; USGS, 2002) | | | | | | | | | | |
| Bristol Dry Lake | 51.7 | 1.7 | 44.7 | 1.8 | 0.0 | 0.0 | 0.1 | 0.0 | 0.0 | 0.0 | 0.0 |
| Mono Lake | 39.4 | 0.0 | 0.0 | 0.0 | 12.8 | 3.1 | 0.0 | 0.0 | 44.4 | 0.02 | 0.3 |
| Salton Sea | 69.4 | 0.0 | 0.0 | 0.0 | 5.4 | 0.7 | 7.8 | 16.2 | 0.0 | 0.0 | 0.5 |
| Seawater | 77.4 | 1.7 | 0.0 | 11.2 | 0.0 | 0.0 | 3.4 | 5.9 | 0.0 | 0.0 | 0.4 |

## 1.2 Research Question

Redox reactions are considered complex with varying degrees of possible mineralogical outcomes. Iron as an element is deemed to be important in the whole process and understanding its geochemical behavior in lacustrine settings is crucial in sediment mineralogy.

The primary objective is;

- To simulate reduction conditions experimentally in sulfide/sulfate and carbonate brine environments to understand the reduction processes iron minerals undergo in lake sediments.

# 2 MATERIALS AND METHODS

## 2.1 Ferrihydrite Synthesis

The ferrihydrite used in this study was synthesized at Georgia State University, Environmental Geochemistry laboratory using the solvent-deficient method (Smith et al., 2012). 20.25g of $Fe(NO_3)3.9H_2O(s)$ and 11.91g of $NH_4HCO_3(s)$ was ground using a pestle and mortar for about 15 minutes (Figure 2-1) producing a slurry mixture which was centrifuged. The resultant precipitate, $5Fe_2O_3.9H_2O$, was oven dried at 100º C for 24 hours. The synthesized ferrihydrite was then stored and labelled accordingly in a clear polystyrene plastic vial. 2 grams of ferrihydrite was observed under a light microscope with magnification x10, where clay- and silt-sized mineral grains were observed.

…

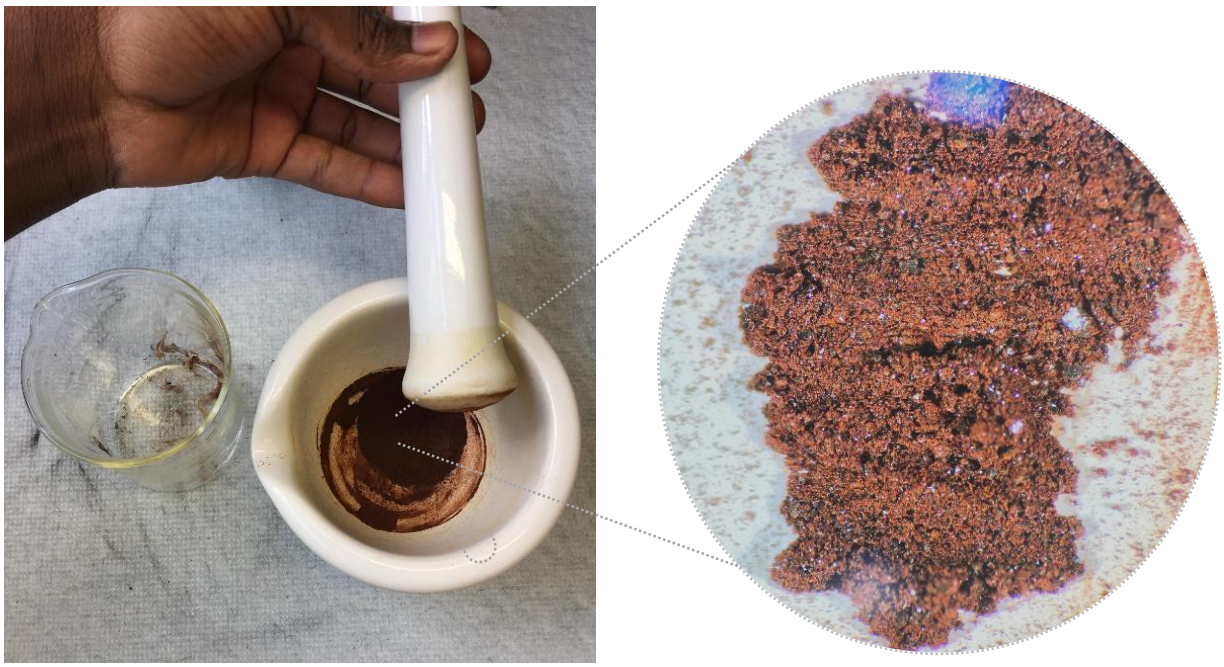

*Figure 2-1 Synthesis of ferrihydrite. [A]. Mixing $Fe(NO_3)_3.9H_2O(s)$ and $NH_4HCO_3(s)$ and [B]. Microscopic view of ferrihydrite.*

## 2.2 Solution Preparation

### *2.2.1 Lake Bogoria ($CO_3^{2-}$ rich solution)*

To simulate Lake Bogoria setting 1*M* of $NaHCO_3$ was prepared by adding 84 grams of $NaHCO_3$ in 1 liter of deionized water in a volumetric flask and stirred thoroughly.

### *2.2.2 Aral Sea ($SO_4^{2-}$ rich solution)*

Hypothetically simulating a $SO_4^{2-}$ rich, Aral Sea, 1*M* of $Na_2SO_4$ was prepared by adding 142.04 grams of $Na_2SO_4$ in a volumetric flask and stirred thoroughly.

### *2.2.3 $S^{2-}$ rich solution*

Simulating the $S^{2-}$ rich environment, 78.04 grams of $Na_2S$ was mixed with 1 liter of deionized water to form 1*M* solution.

## 2.3 Laboratory setup and general measurements.

### *2.3.1 pH measurement of $CO_3^{2-}$/ $SO_4^{2-}$/ $S^{2-}$ rich solution.*

The Sper Scientific 860031 benchtop pH and mV meter was used for measuring the pH of the solutions. Calibration of the pH meter was achieved using standard Atlas Scientific, Environmental Robotics buffer solutions of pH values 4, 7, and 10 accordingly. The pH meter sensor probe was standardized in oxygenated water and the measurements were not taken in situ during anaerobic reactions. The probe tip (glass bulb) was completely immersed into the sample and gently stirred creating a well-mixed solution. Readings were taken after stabilization and the word “READY” was illuminated on the display. Four pH measurements were taken for each brine solution.


*Figure 2-2 pH meter apparatus used for determining the pH of the brines.*

### *2.3.2 Reacting reduced mobile $Fe^{2+}$ with $CO_3^{2-}$ / $SO_4^{2-}$ / $S^{2-}$ rich solutions.*

Forty milliliters of $CO_3^{2-}$/ $SO_4^{2-}$/ $S^{2-}$ lab simulated waters was placed in a vacuum flask and one hundred milligrams of ferrihydrite added and resultant mixture purged with Nitrogen gas for about five minutes. Two hundred milligrams of Na-dithionite [$Na_2S_2O_4$] was immediately added to the mixture. The experiment was conducted at a steady temperature of 70°C for various time intervals of one hour, two hours, three hours, four hours, twenty-four hours and thirty hours and continuously stirred at 350 revolutions per minute (rpm) for homogeneity. Reduction times for different batches of the experiment varied from fifteen minutes to several hours (Tables 2-1 and 2-2). The resulting precipitates were then filtered using 0.45µm filter paper and dried overnight undisturbed. Experiments RG1_$CO_3^{2-}$ and RG2_$CO_3^{2-}$, were conducted using different parameters of four hundred milligrams of $Na_2S_2O_4$ and twenty-four hours and thirty hours respective time durations. The equipment setup was simplified from a well-known ferrihydrite reduction process (Stucki et al., 1984).

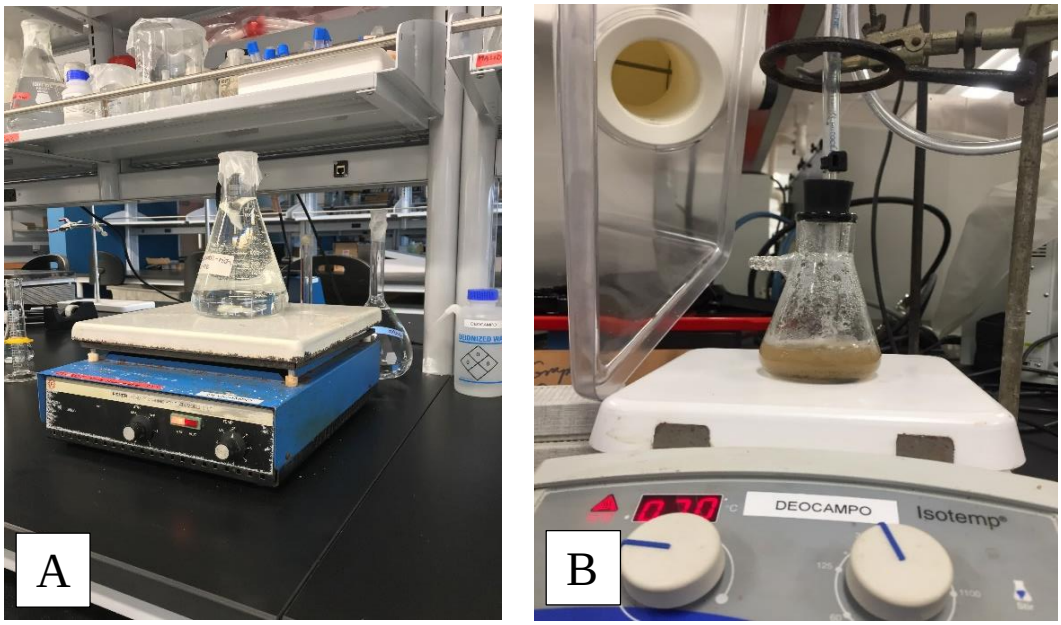


*Figure 2-3. Ferrihydrite reduction. [A]. Stirring brine thoroughly for homogeneity and [B]. Reacting ferrihydrite with $Na_2S_2O_4$ under inert conditions, $N_2(g)$ purged.*

*Table 2-1 $CO_3^{2-}$-rich simulation parameters.*

| Experiment 1. $CO_3^{2-}$ rich solution. | | | | Experiment 2. $CO_3^{2-}$ rich solution. | | | |
|---|---|---|---|---|---|---|---|
| ID | Temps (°C) | Revolutions (rpm) | Time(hours) | ID | Temps (°C) | Revolutions (rpm) | Time (hours) |
| MC1_ $CO_3^{2-}$ | 70 | 350 | 1 | M1_ $CO_3^{2-}$ | 70 | 350 | 1 |
| MC2_ $CO_3^{2-}$ | 70 | 350 | 2 | M2_$CO_3^{2-}$ | 70 | 350 | 2 |
| MC3_ $CO_3^{2-}$ | 70 | 350 | 3 | M3_ $CO_3^{2-}$ | 70 | 350 | 3 |
| MC4_ $CO_3^{2-}$ | 70 | 350 | 4 | M4_ $CO_3^{2-}$ | 70 | 350 | 4 |
| RG1_ $CO_3^{2-}$ | 70 | 350 | 24 | | | | |
| RG2_ $CO_3^{2-}$ | 70 | 350 | 30 | | | | |

*Table 2-2 Sulfate and sulfide-rich simulation parameters.*

| Experiment 1. $SO_4^{2-}$ rich solution. | | | | Experiment 2. $S^{2-}$ rich solution. | | | |
|---|---|---|---|---|---|---|---|
| ID | Temps (°C) | Revolutions (rpm) | Time(hours) | ID | Temps (°C) | Revolutions (rpm) | Time (hours) |
| MC1_ $SO_4^{2-}$ | 70 | 350 | 1 | M1_$S^{2-}$ | 70 | 350 | 1 |
| MC2_ $SO_4^{2-}$ | 70 | 350 | 2 | M2_$S^{2-}$ | 70 | 350 | 2 |
| MC3_ $SO_4^{2-}$ | 70 | 350 | 3 | M3_ $S^{2-}$ | 70 | 350 | 3 |
| MC4_ $SO_4^{2-}$ | 70 | 350 | 4 | M4_$S^{2-}$ | 70 | 350 | 4 |

## 2.4 XRD (X-Ray Powder Diffraction) mineral identification

The PANalytical X'Pert Pro situated in the Environmental Geochemistry lab, Georgia State University was used for XRD measurements. Three to six grams of resultant mineral precipitate was mounted on metallic discs, which provide a stable surface for analysis. The samples were then scanned from 4 to 60 degrees 2Θ (two theta). The graphite monochromator was in place to cancel interference components such as fluorescent X-rays from the sample and $K_\beta$-rays from the Cu target. A copper anode was used for supplying an incident beam of Cu Kα X-rays. The irradiated length of the sample is 10mm, receiving slit size of 0.1". Reasonable differences in the relative crystallinities were observed from the variances in peak heights and widths in the XRD patterns. Mineral identification of the samples was achieved after several measurements using peak-match capabilities.

## 2.5 Mineral Crystallite Size Calculation.

Using the XRD data, crystallite sizes for the mineral precipitates were calculated and averaged using the Scherrer's equation (Patterson, 1939) (See equation 2-1).

$$\text{Crystallite size, } D_p = K\,l / (B \cos q) \quad \ldots \text{ Equation 2-1}$$

Where;

$D_p$ = Average crystallite size (nm)

K = Scherrer constant (K varies from 0.68 to 2.08; K = 0.94 for spherical crystallites with cubic symmetry)

l = X-Ray wavelength, Cu Kα average = 1.54178 Å

B = FWHM (Full Width at Half Maximum) of XRD peak.

q = XRD peak position, one half of 2q.

The resulting crystallite sizes were then compared to varying time durations in hours.

## 2.6 Aqueous Geochemical Modelling, PHREEQ.

The equilibrium concentrations of dissolved chemical species and their saturation degree (saturation index) of solid phases in equilibrium within the solution, were determined using the geochemical modeling application WEB-PHREEQ (Parkhurst and Appelo, 1999).

The saturation index (SI) calculated by comparing the ion activities of dissolved mineral ions (IAP) with their solubility product ($K_{sp}$). SI = $Log_{10}$ (IAP/$K_{sp}$). SI = 0 implies saturated (in equilibrium) concerning the mineral, SI > 0 implies super saturation and SI < 0 implies under saturation.

The following steps were taken using the PHREEQ modelling program;

1. Select the simple speciation option.
2. Single solution selection as our next parameter.
3. And the PHREEQC database as our point of reference.
4. Under the "Environmental conditions" section. The earlier calculated pH values are used with the option of having the pH fixed. The temperature value used is 70°C.
5. The "Concentration Units" used are "moles/liter".
6. Under the "Major and commonly analyzed elements", calculated values of Na, Fe(II), $CO_3^{2-}$ and $SO_4^{2-}$ were inserted in their respective fields according the conducted simulation.
7. The full output file was generated using PHREEQ upon pressing the "Continue" tab.
8. The saturation index values generated in the report are then plotted against the amount of presumed Fe(II).

## 2.7 Scanning Electron Microscope (SEM) Images.

A Hitachi S-4800 Field Emission? Scanning Electron Microscope (SEM) with secondary electron, backscatter electron, transmission electron detectors and an EDAX energy dispersive X-ray spectrometer (EDS) located in Rutgers University, Department of Chemistry was used to obtain the SEM images presented in this report. Samples were placed onto sample stubs and sputtered by a few nanometers of gold to increase conductivity. Nominal pressures were calibrated in the SEM chamber and the sample stubs placed onto the stage. The operating voltage used was 20 kV. Data collected in the form of two-dimensional images was generated and captured at different magnification levels ranging from 1x to 10kx. Variations in textural and chemical characterizations of the samples was noted.

# 3 RESULTS

## 3.1 XRD (X-Ray Powder Diffraction)

### *3.1.1 Ferrihydrite identification*

The prepared ferrihydrite sample was collected and analyzed using a PANalytical X'Pert Pro diffractometer. XRD measurements were conducted over a 20 – 80°, 2Θ range and two broad diffraction peaks of values 1.9780Å and 1.4734Å were observed; this diffraction pattern corresponded to the known 2-line ferrihydrite (Figure 3-1). Per this diffraction pattern, ferrihydrite is thought to be composed of spherical particles of poorly aggregated crystalline Fe (III) oxyhydroxides, which was also observed in the microscopic view.

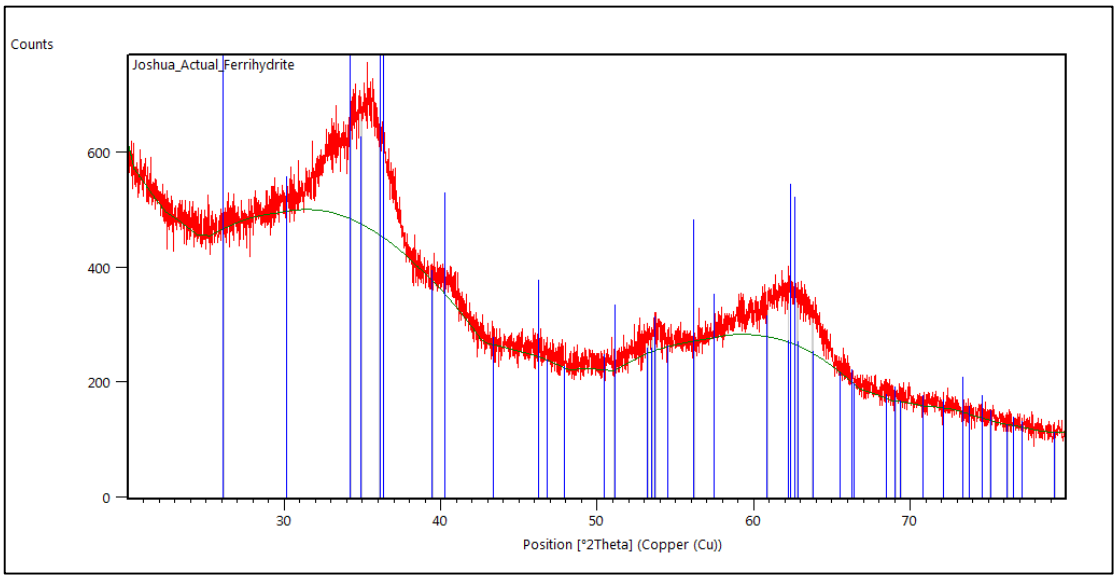


*Figure 3-1 XRD analysis conducted on the ferrihydrite sample.*

### *3.1.2 Mineral Precipitate Identification.*

Mineral precipitates from the lab simulations of reacting ferrihydrite with the $CO_3^{2-}$/ $SO_4^{2-}$/ $S^{2-}$ brine solutions were analyzed using the XRD method. From the carbonate and sulfate brine reactions the minerals siderite and magnetite were identified respectively for the different time variations based on the distribution of the diffraction peaks (Figures 3-2, 3-3, 3-4 and 3-5). The magnetite was confirmed by using a magnet. No particular sulfide mineral resulting from the sulfide simulation could be identified under the XRD. For the 30 hours carbonate simulation using 400mg of Na- dithionite, traces of goethite in addition to siderite is present.

*Table 3-1. Summary of observed minerals and treatments.*

| **Sample(s)** | **Treatments done** | **Analytical Methods Used** | **Observed Minerals** |
|---|---|---|---|
| Carbonate simulation samples (MC1_$CO_3^{2-}$, MC2_$CO_3^{2-}$, MC3_$CO_3^{2-}$, MC4_$CO_3^{2-}$) | - 200mg of Na-dithionite.<br>- 100mg of Ferrihydrite.<br>- Nitrogen gas purged.<br>- 70°C temperatures | - X-Ray Diffractometer.<br>- Scanning Electron Microscopy.<br>- PHREEQ Geochemical modelling | Siderite, Goethite, Chikanovite (?) |
| Sulfate simulation samples (MC1_$SO_4^{2-}$,MC2_$SO_4^{2-}$, MC3_$SO_4^{2-}$, MC4_$SO_4^{2-}$) | | | Magnetite |
| Sulfide simulation samples (MC1_$S^{2-}$,MC2_$S^{2-}$, MC3_$S^{2-}$, MC4_$S^{2-}$) | | | No specific identifiable mineral observed. |
| Carbonate simulation samples (RG1_$CO_3^{2-}$, RG2_$CO_3^{2-}$) | - 400mg of Na-dithionite.<br>- 100mg of Ferrihydrite.<br>- Nitrogen gas purged.<br>- 70°C temperatures | | Siderite, Goethite, |

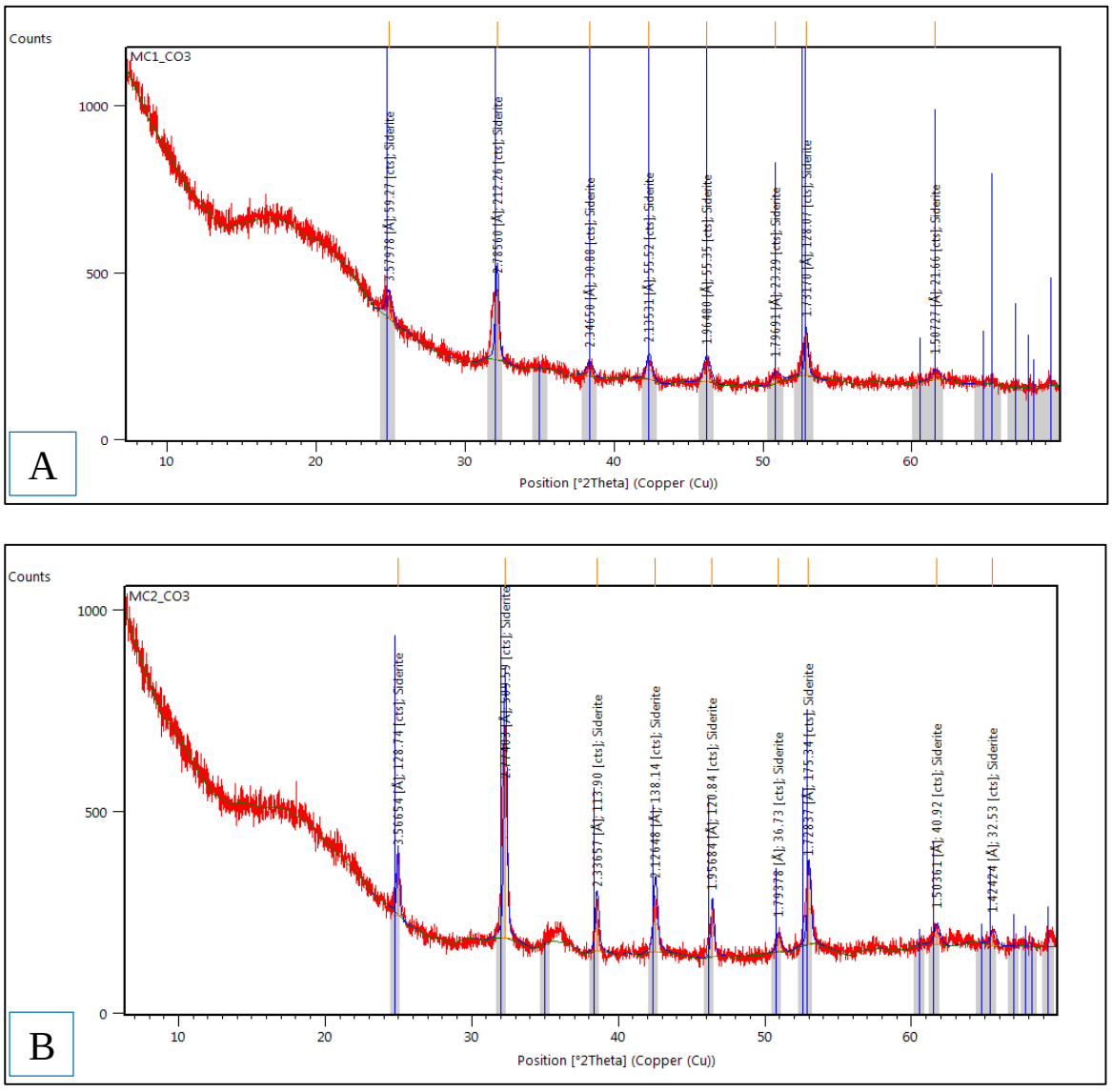


*Figure 3-2 XRD graphs of mineral precipitates. [A] 1hour carbonate simulation and [B] 2 hours carbonate simulation.*

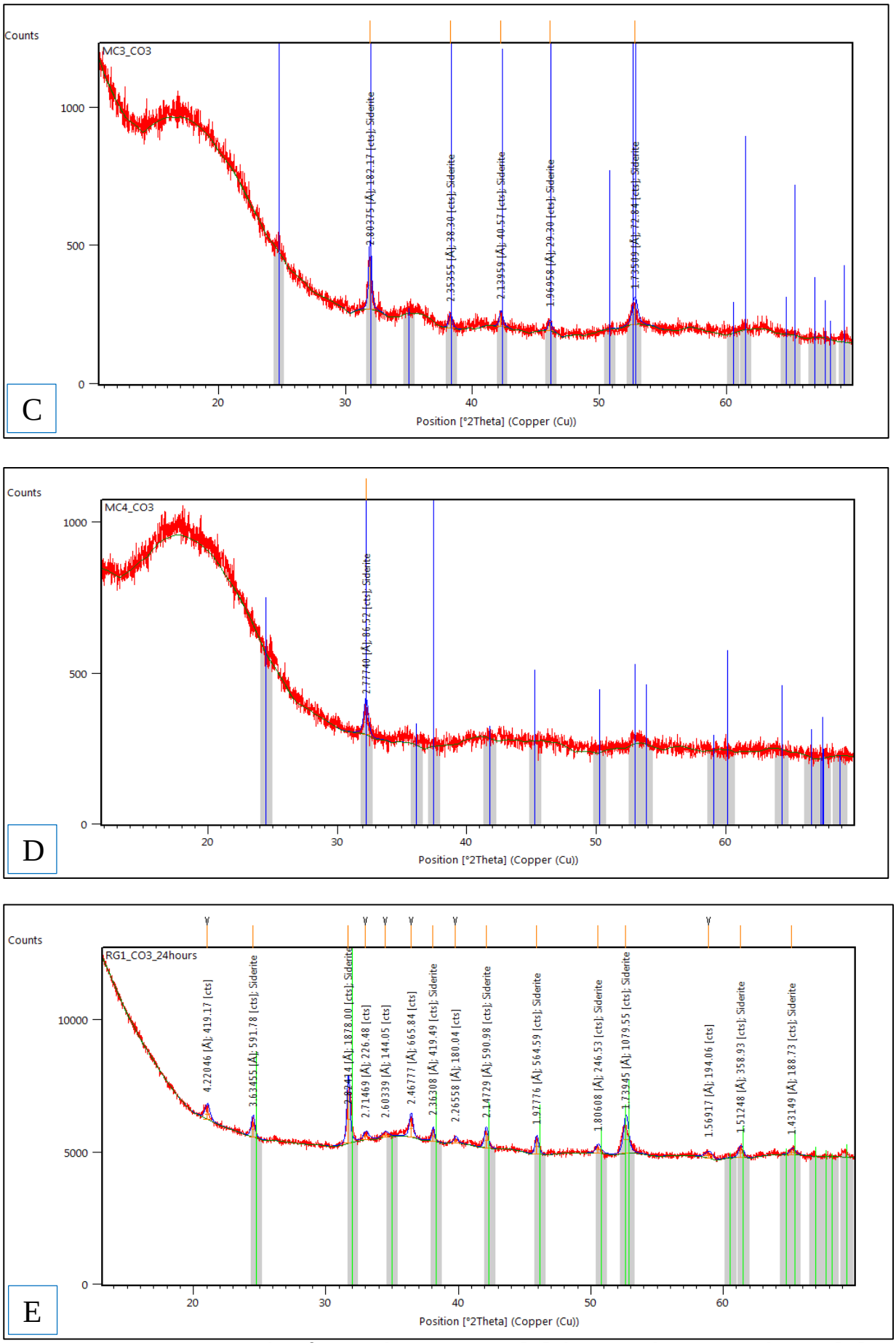


*Figure 3-3 XRD graphs of mineral precipitates. [C]3hours carbonate simulation, [D] 4 hours carbonate simulation and [E] 24 hours carbonate simulation.*

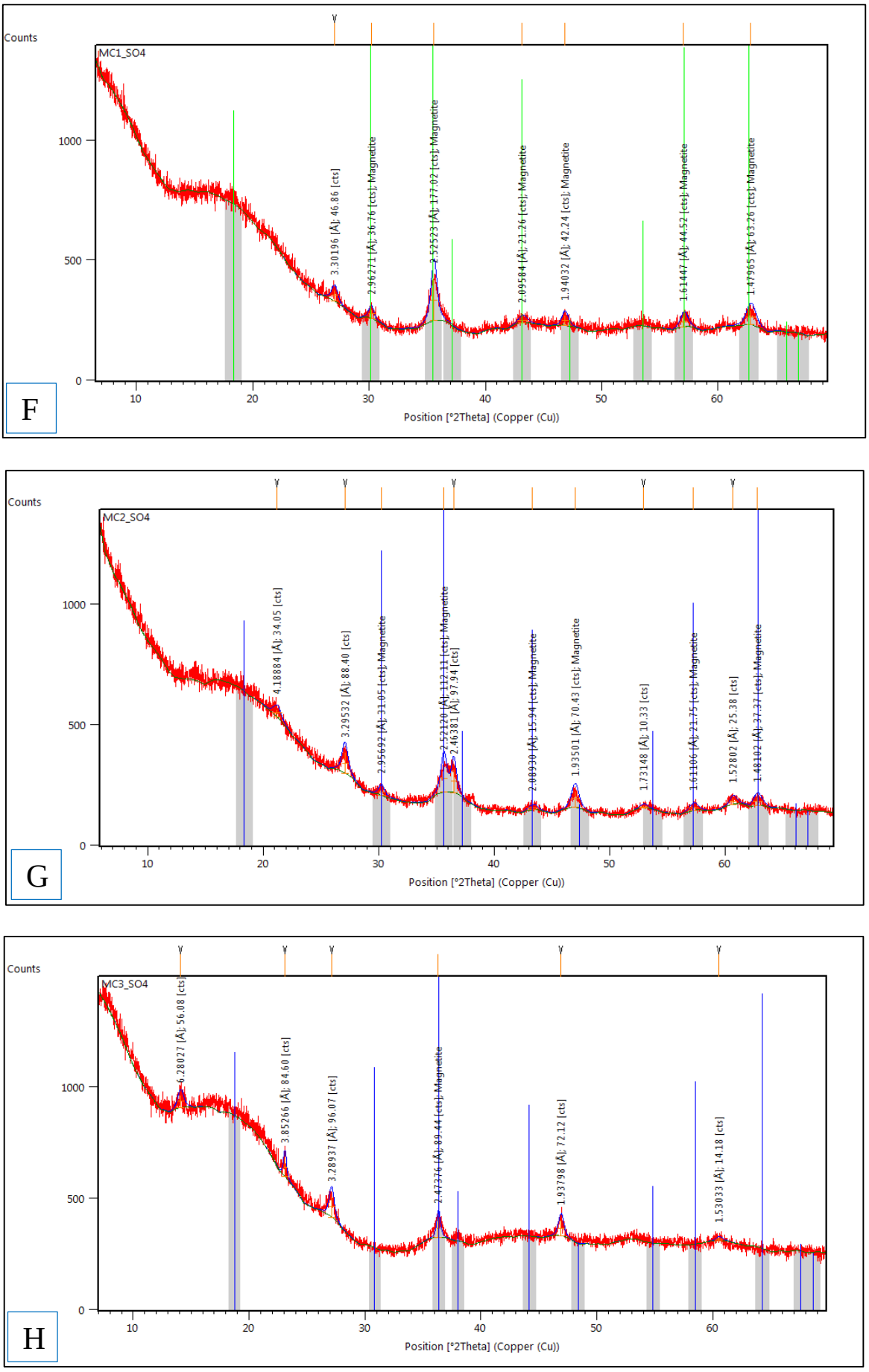


*Figure 3-4 XRD graphs of mineral precipitates. [F]1hour, [G] 2 hours and [H] 3 hours sulfate simulations.*

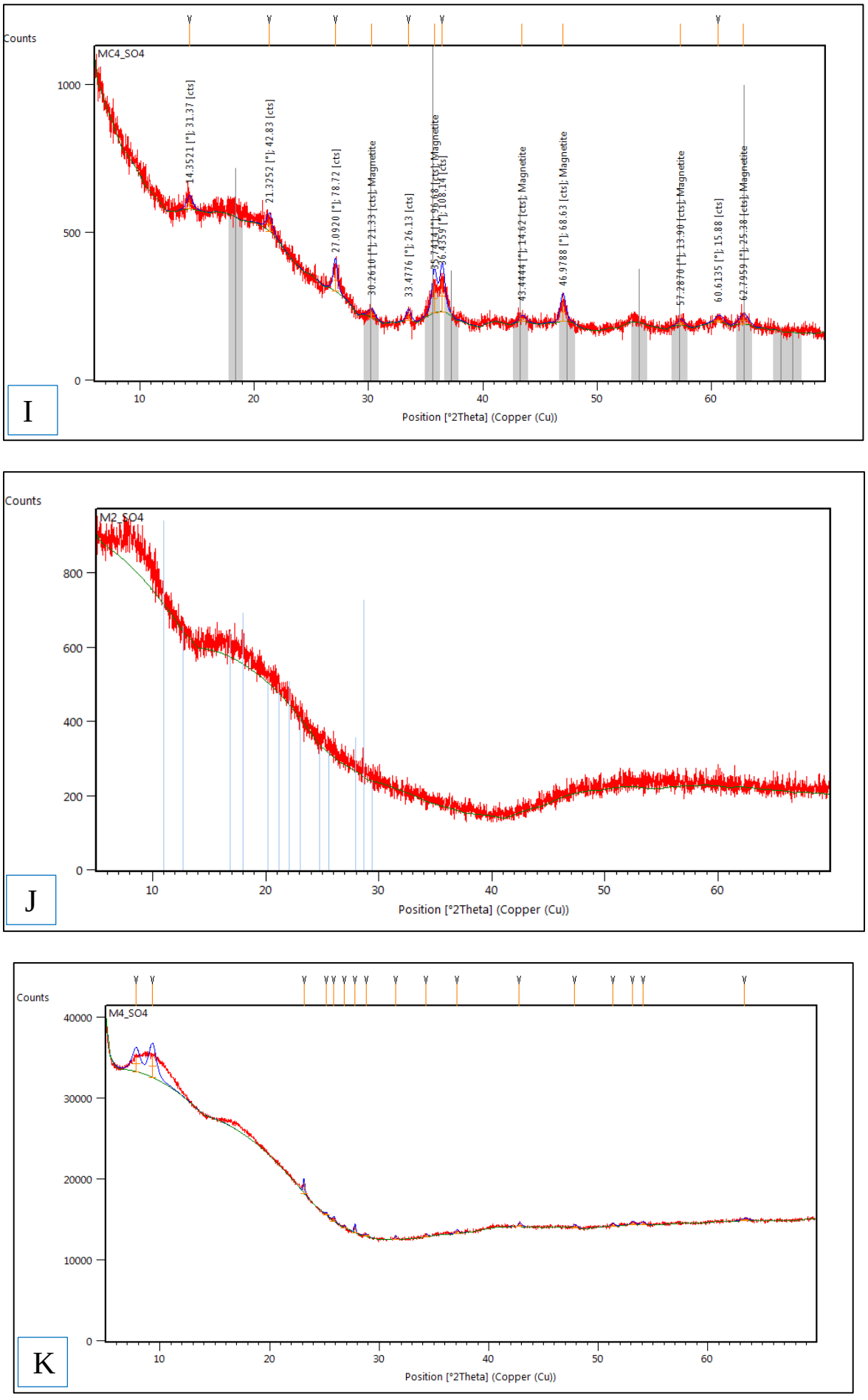


*Figure 3-5 XRD graphs of mineral precipitates. [I] 4hours sulfate simulations, [J] 2 hours and [K] 4 hours sulfide simulations.*

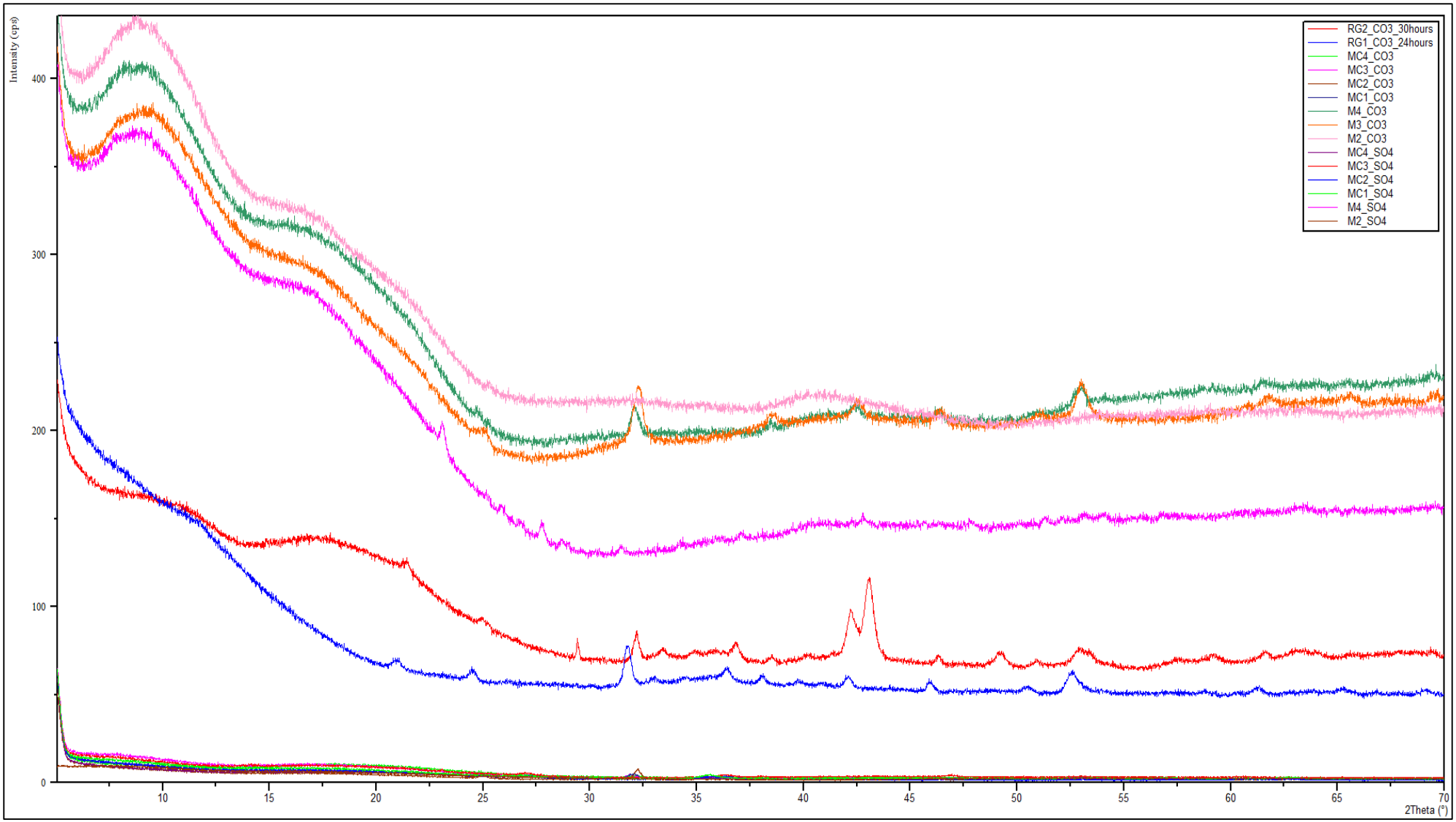


*Figure 3-6 A combined XRD graph with all the simulations.*

### 3.2 pH measurements

Four pH measurements were recorded and averaged for the carbonate, sulfate and sulfide solutions. The average measurements were 8.4, 13.4 and 12.2 for the respective brines. The sulfate and sulfide solutions were noted to be highly basic in nature.

*Table 3-2 pH solution measurements.*

| No. of Attempts | Carbonate solution pH measurement. | Sulfate solution pH measurement. | Sulfide solution pH measurement. |
|---|---|---|---|
| 1 | 8.3 | 13.3 | 12.2 |
| 2 | 8.4 | 13.4 | 12.2 |
| 3 | 8.4 | 13.5 | 12.3 |
| 4 | 8.5 | 13.4 | 12.2 |
| **Average pH measurements** | **8.4 ± 0.1** | **13.4 ± 0.1** | **12.2 ± 0.1** |

### 3.3 Scanning Electron Microscope (SEM) Images.

Mineral precipitates resulting from the simulation of the $CO_3^{2-}$/ $SO_4^{2-}$/ $S^{2-}$ brine solutions were analyzed using the SEM method. Several minerals were clearly identified under the SEM images. Spherules of varying diameters, between one to two nanometers, from the carbonate simulations are observed and identified as siderite (Figure 3.7 [a-d]). Platy-structured mineral flakes appear in close association with the siderite, identified as Chukanovite, based on their habit.

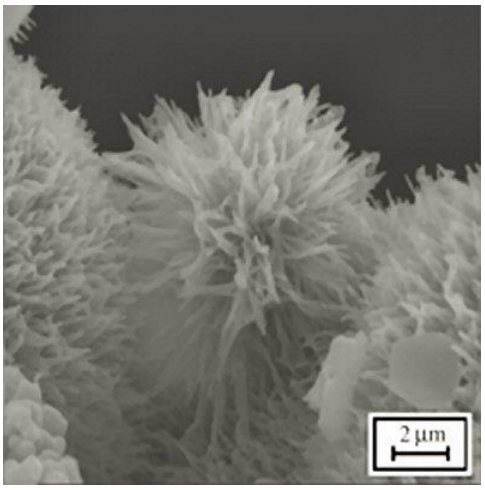


*Figure 3-7. Chukanovite SEM image. (Berner, 1981)*

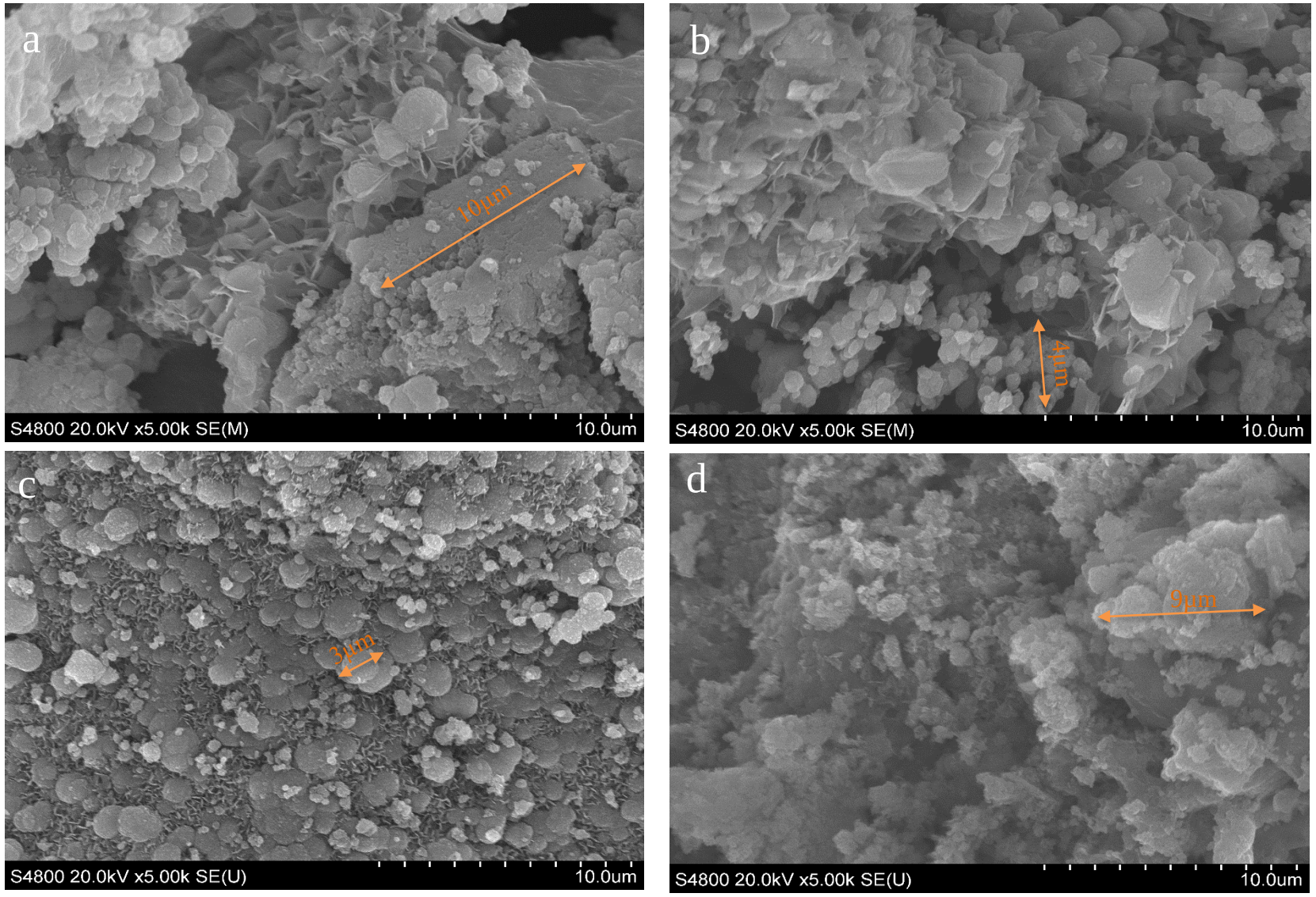


*Figure 3-8 SEM images of carbonate simulations for [a] 1hour, [b] 2 hours, [c] 3 hours and [d] 4 hours.*

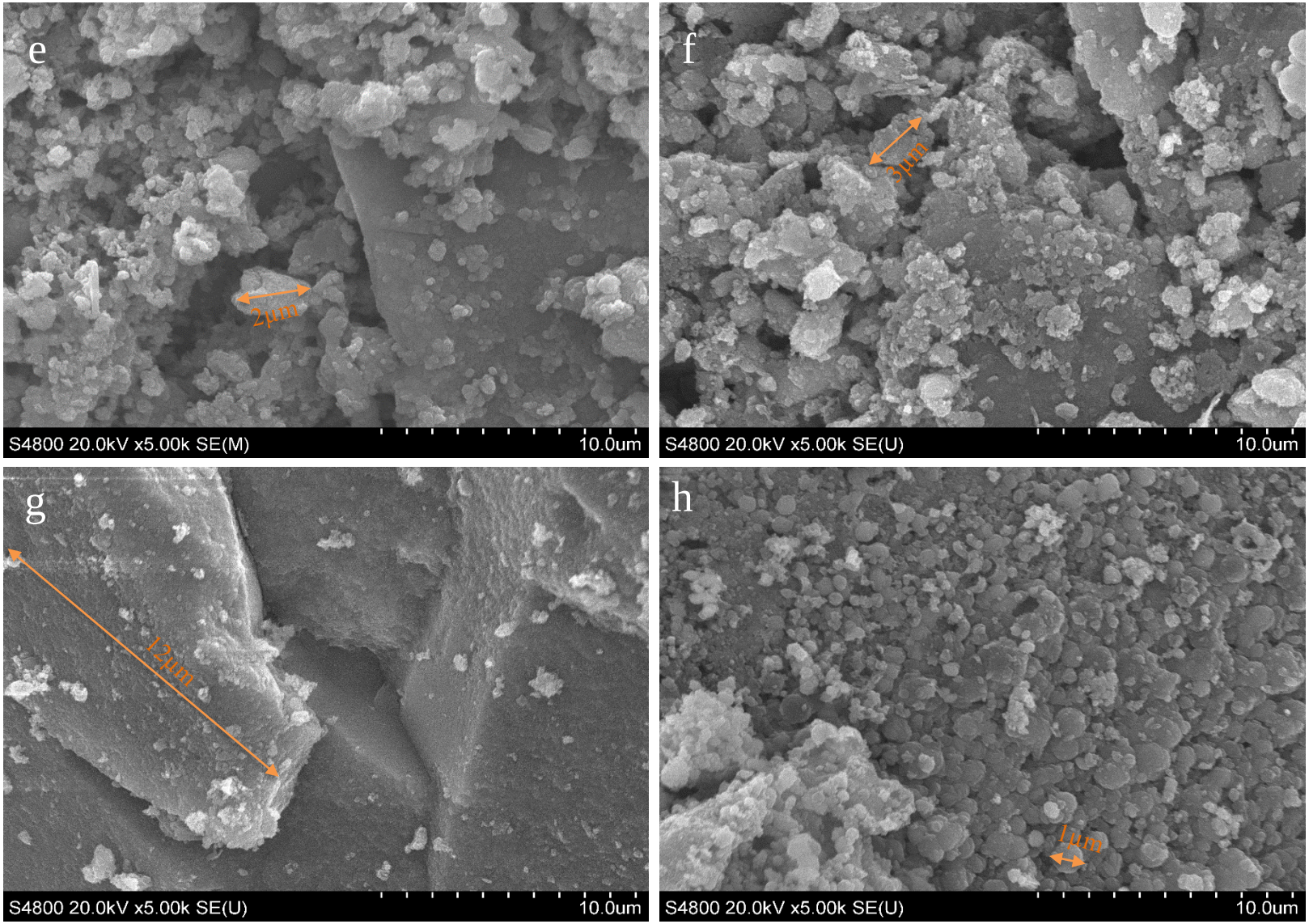


*Figure 3-9 SEM images of sulfate simulations for [e] 1hour, [f] 2 hours, [g] 3 hours and [h] 4 hours*

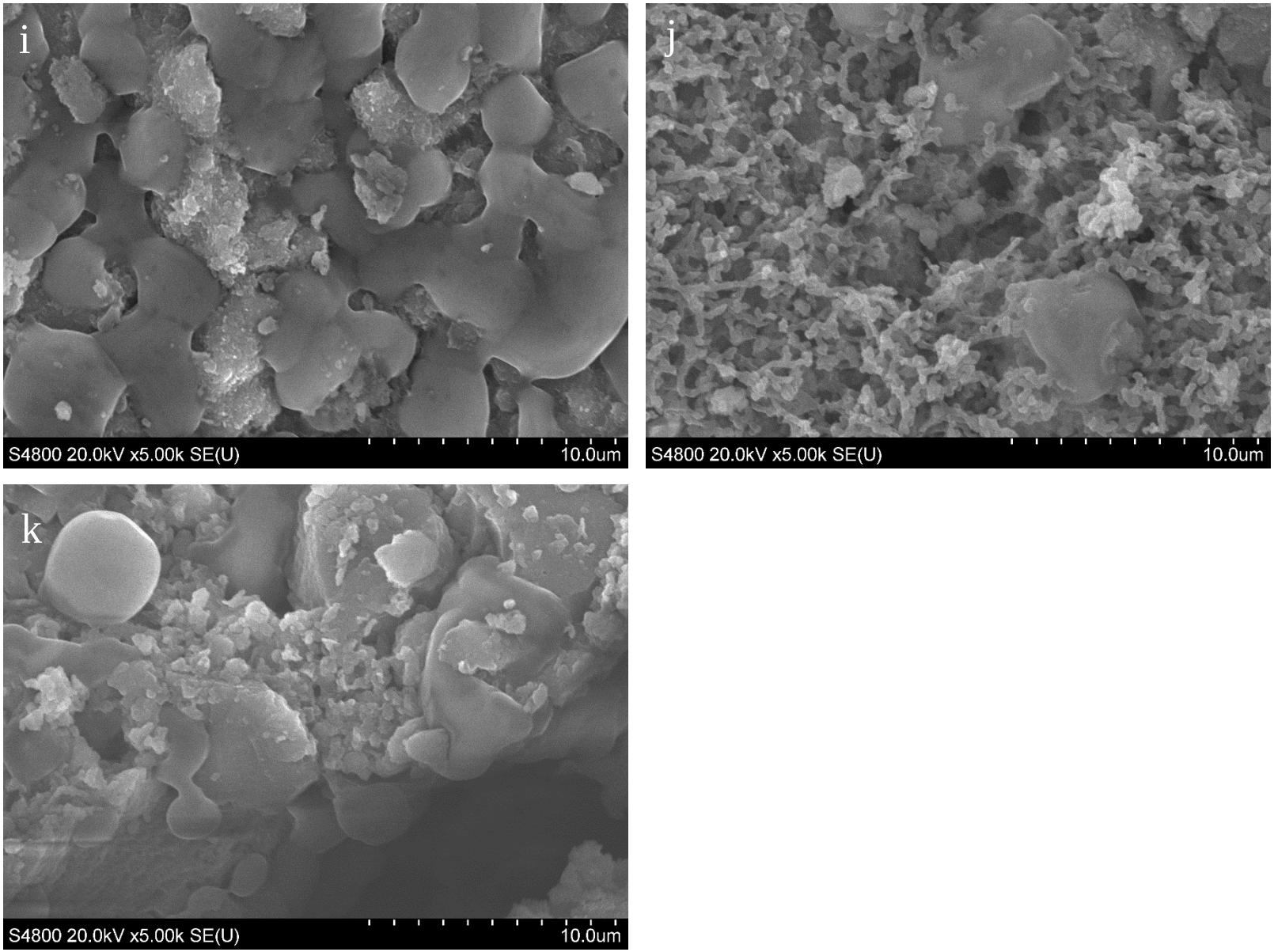


*Figure 3-10 SEM images of sulfide simulations for [i]2hours, [j] 3 hours and [k] 4 hours.*

## 3.4 Aqueous Geochemical Modelling, PHREEQ

Geochemical simulations were conducted using the PHREEQ program. The iron (II) content values were incrementally adjusted respective to the different brine simulations to observe the behavior of the mineral saturation index. The saturation index is then plotted against the iron content.

### *3.4.1 $CO_3^{2-}$ rich simulation.*

Projected $Fe^{2+}$ measurements were inputs into the PHREEQ geochemical modelling program to calculate the saturation indexes for the expected mineral formations. The final mineral product for the carbonate simulation was noted as siderite. Siderite? Saturation Index was plotted against the $Fe^{2+}$ content.

*Table 3-3 Table showing projected and actual $Fe^{2+}$ and siderite saturation index.*

| X ($Fe^{2+}$ mol/l) | Y (Siderite Saturation Index) |
|---|---|
| 0.00001 | 1.41 |
| 0.0001 | 2.41 |
| 0.001 | 3.39 |
| 0.002 | 3.68 |
| 0.005 | 4.02 |
| 0.007 | 4.12 |
| 0.009 | 4.19 |
| 0.02 | 4.35 |
| 0.05 | 4.43 |
| 0.07 | 4.45 |
| 0.1 | 4.47 |

| Actual simulation measurements taken | |
|---|---|
| X ($Fe^{2+}$ mol/l) | Y (Siderite Saturation Index) |
| 0.001193324 | 3.47 |

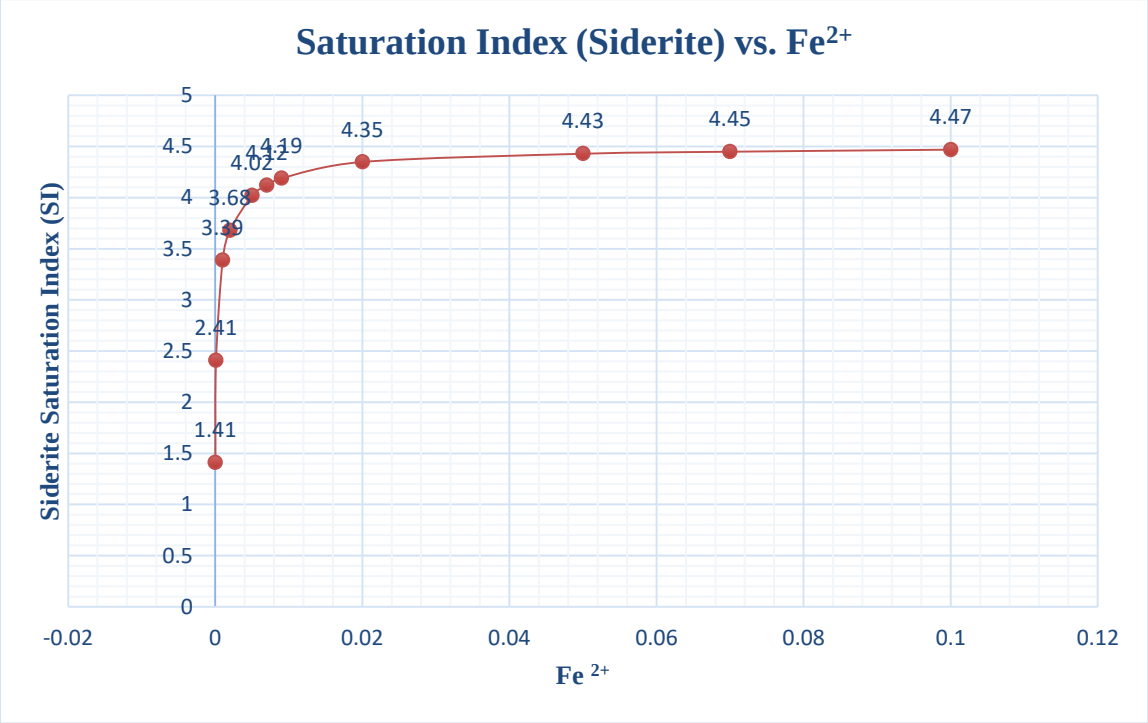


*Figure 3-11 Graph displaying relationship between Iron (II) content versus Siderite saturation index.*

The relationship between the two parameters is directly proportional but becomes tangential with increased iron (II) content (see Figure 3.10)

### *3.4.2 $SO_4^{2-}$ rich simulation.*

*Table 3-4. Table showing projected and actual $Fe^{2+}$ and pyrite saturation index.*

| X ($Fe^{2+}$ mol/l) | Y (Pyrite Saturation Index) |
|---|---|
| 0.00001 | 0.41 |
| 0.0001 | 3.31 |
| 0.001 | 3.72 |
| 0.002 | 3.76 |
| 0.005 | 3.81 |
| 0.007 | 3.87 |
| 0.009 | 3.9 |
| 0.02 | 3.95 |
| 0.05 | 4.02 |
| 0.07 | 4.06 |
| 0.1 | 4.1 |

| Actual Simulation measurements | |
|---|---|
| **X ($Fe^{2+}$ mol/l)** | **Y (Pyrite Saturation Index)** |
| 0.00689848 | 3.86 |

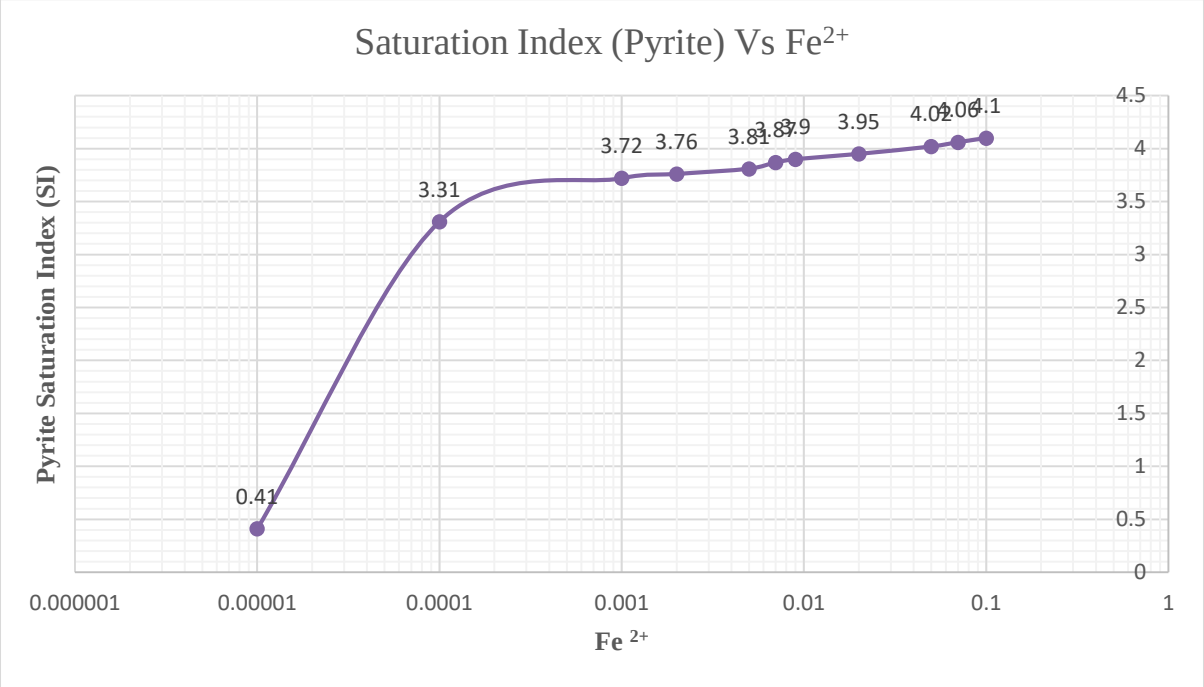


*Figure 3-12. Graph displaying relationship between Iron (II) content Vs Pyrite saturation index.*

## 3.5 Mineral Crystallite Size Calculation

Using Scherrer's equation (Patterson, 1939), the average crystallite sizes for the mineral precipitates from the simulations were calculated using the following formulae;

$$\text{Crystallite size, } D_p = K \mathbf{l} / (B \cos \Theta) \ldots \text{Equation 3-5}$$

Where;

$\mathbf{D_p}$ = Average crystallite size (nm).

**K** = Scherrer Constant (K varies from 0.68 to 2.08; K = 0.94 for spherical crystallites with cubic symmetry).

**l** = X-Ray wavelength, Cu Kα = 1.54178 Å.

**B** = FWHM (Full Width at Half Maximum) of XRD peak (Δ2Θ), radians.

Θ = XRD peak position, one half of 2Θ .

The crystallite sizes were calculated for each mineral precipitate (siderite, magnetite) in every simulation and averaged. Typically, sub-micrometer sized measurements are used. The Microsoft excel formula used was;

**(0.9*0.15418) / Radians (FWHM Left [°2Θ]) * Cos (Radians ([°2Θ]) / 2))**

The resultant average mineral crystallite sizes for the simulations were plotted against time duration in hours (Figures 3.11 and 3.12). FWHM and peak positions used in the crystallite size calculations were generated by HighScore Plus, an XRD analysis software.

The carbonate simulations were simulated twice. The average crystallite sizes plotted against time in hours are directly proportional in both simulations, with the peak sizes at 2 hours and 3 hours respectively which gradually declined with time. (see Figure 3.12 and 3.13) The crystallite sizes were calculated using Microsoft Excel Spreadsheet 2016 (Tables 3-4 to 3-8).

*Table 3-5. Average crystallite size for 2 hours $CO_3^{2-}$ simulation.*

| Pos. [°2Θ] | FWHM Left [°2Θ] | Crystallite Size (nm) | Average Crystallite Size (nm) |
|---|---|---|---|
| 7.792 | 0.614 | 12.919 | 16.143 |
| 8.756 | 0.409 | 19.368 | |

*Table 3-6. Average crystallite size for 3 hours $CO_3^{2-}$ simulation*

| Pos. [°2Θ] | FWHM Left [°2Θ] | Crystallite Size (nm) | Average Crystallite Size (nm) |
|---|---|---|---|
| 25.133 | 0.409 | 18.959 | 18.098 |
| 32.300 | 0.461 | 16.584 | |
| 38.519 | 0.307 | 24.448 | |
| 42.543 | 0.307 | 24.133 | |
| 46.452 | 0.409 | 17.850 | |
| 51.047 | 0.409 | 17.529 | |
| 53.019 | 0.409 | 17.382 | |
| 61.760 | 0.409 | 16.671 | |
| 65.609 | 0.716 | 9.328 | |

*Table 3-7. Average crystallite size for 4 hours $CO_3^{2-}$ simulation*

| Pos. [°2Θ] | FWHM Left [°2Θ] | Crystallite Size (nm) | Average Crystallite Size (nm) |
|---|---|---|---|
| 32.068 | 0.409 | 18.669 | 17.026 |
| 38.420 | 0.307 | 24.455 | |
| 40.388 | 0.819 | 9.114 | |
| 42.451 | 0.409 | 18.107 | |
| 46.310 | 0.409 | 17.860 | |
| 53.099 | 0.358 | 19.855 | |
| 61.608 | 0.614 | 11.122 | |

*Table 3-8. Average crystallite size for 3 hours $CO_3^{2-}$ simulation. Second attempt.*

| Pos. [°2Θ] | FWHM Left [°2Θ] | Crystallite Size (nm) | Average Crystallite Size (nm) |
|---|---|---|---|
| 7.880 | 0.614 | 12.918 | 21.788 |
| 31.920 | 0.256 | 29.883 | |
| 38.242 | 0.307 | 24.469 | |
| 42.240 | 0.307 | 24.158 | |
| 46.086 | 0.307 | 23.831 | |
| 52.760 | 0.461 | 15.467 | |

*Table 3-9. Average crystallite size for 4 hours $CO_3^{2-}$ simulation. Second attempt*

| Pos. [°2Θ] | FWHM Left [°2Θ] | Crystallite Size (nm) | Average Crystallite Size (nm) |
|---|---|---|---|
| 32.204 | 86.520 | 0.088 | 0.088 |

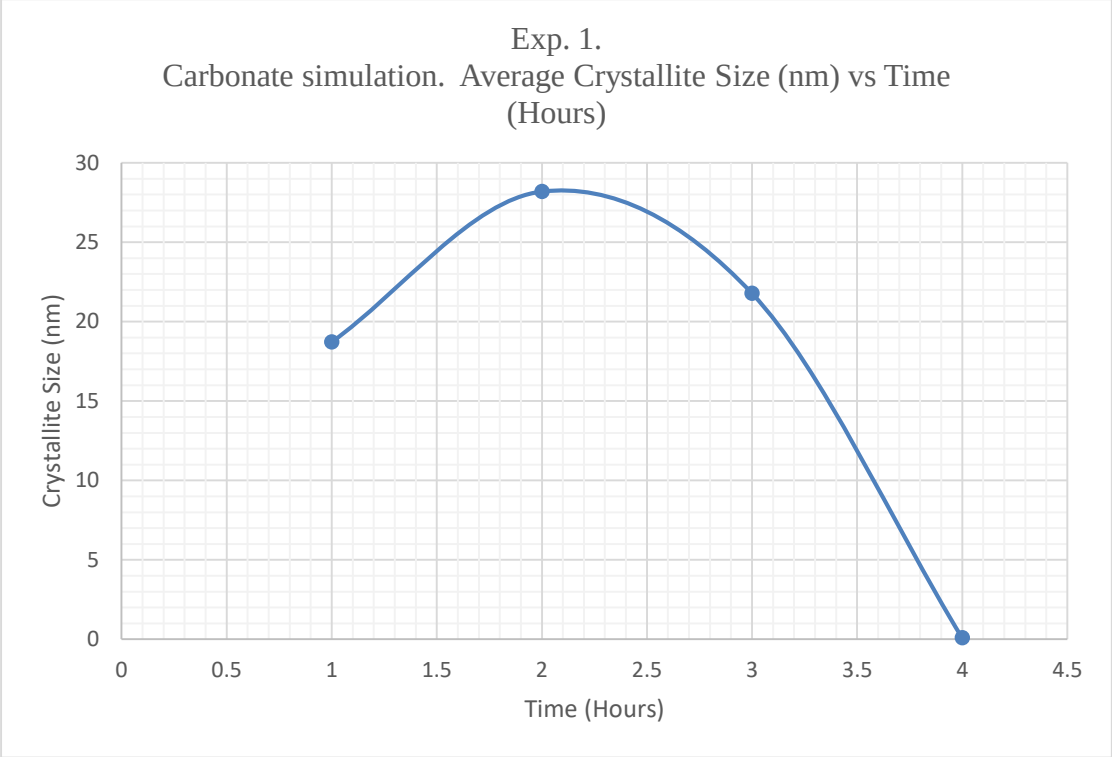


*Figure 3-13 Graph displaying average crystallite size (nm) vs time in hours. 1st carbonate simulation.*

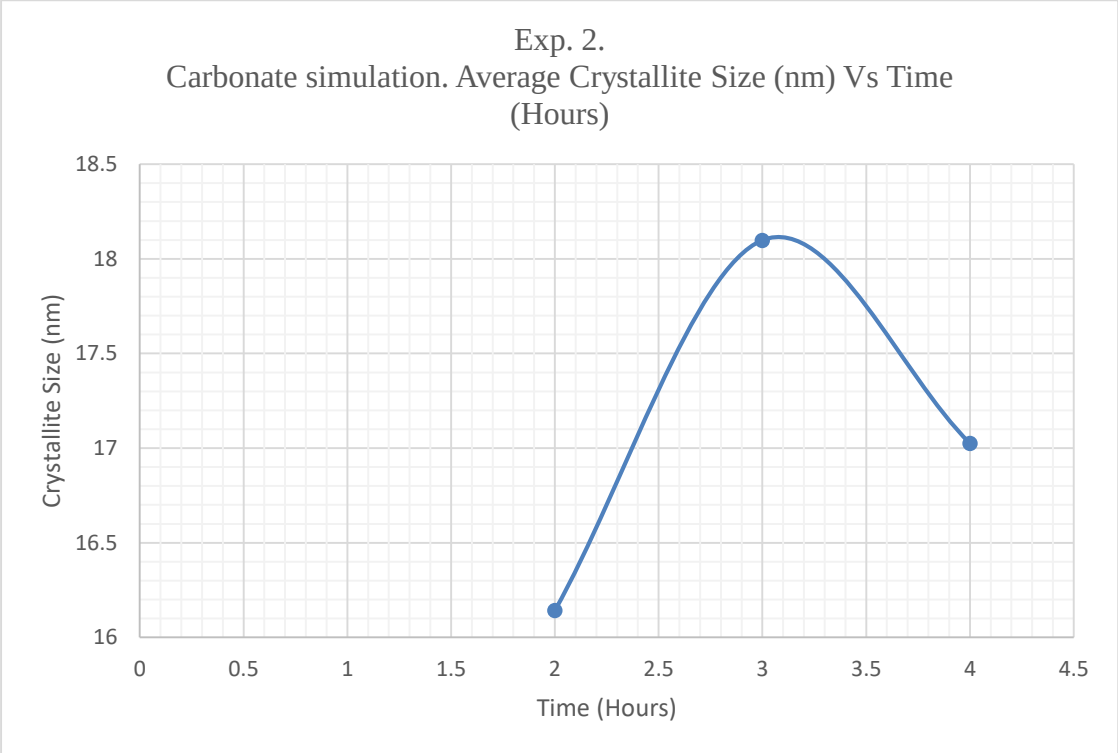


*Figure 3-14 Graph displaying average crystallite size (nm) vs time in hours. 2nd carbonate simulation.*

*Table 3-10. Average crystallite size for 1 hour $SO_4^{2-}$ simulation.*

| Pos. [°2Θ] | FWHM Left [°2Θ] | Crystallite Size (nm) | Average Crystallite Size (nm) |
|---|---|---|---|
| 27.003 | 0.614 | 12.591 | 11.141 |
| 30.165 | 0.511 | 15.023 | |
| 35.551 | 0.614 | 12.330 | |
| 43.165 | 0.818 | 9.038 | |
| 46.822 | 0.614 | 11.883 | |
| 57.046 | 0.716 | 9.756 | |
| 62.802 | 0.921 | 7.368 | |

*Table 3-11. Average crystallite size for 2 hours $SO_4^{2-}$ simulation.*

| Pos. [°2Θ] | FWHM Left [°2Θ] | Crystallite Size (nm) | Average Crystallite Size (nm) |
|---|---|---|---|
| 21.211 | 0.819 | 9.545 | 10.693 |
| 27.059 | 0.614 | 12.589 | |
| 30.226 | 0.614 | 12.501 | |
| 35.611 | 0.614 | 12.328 | |
| 36.469 | 0.512 | 14.757 | |
| 43.307 | 0.819 | 9.026 | |
| 46.958 | 0.716 | 10.179 | |
| 52.878 | 0.819 | 8.695 | |
| 57.178 | 0.819 | 8.527 | |
| 60.601 | 0.614 | 11.180 | |
| 62.737 | 0.819 | 8.292 | |

*Table 3-12. Average crystallite size for 3 hours $SO_4^{2-}$ simulation.*

| Pos. [°2Θ] | FWHM Left [°2Θ] | Crystallite Size (nm) | Average Crystallite Size (nm) |
|---|---|---|---|
| 14.102 | 0.614 | 12.851 | 16.643 |
| 23.086 | 0.307 | 25.374 | |
| 27.109 | 0.512 | 15.105 | |
| 36.317 | 0.358 | 21.090 | |
| 46.882 | 0.512 | 14.255 | |
| 60.500 | 0.614 | 11.186 | |

*Table 3-13. Average crystallite size for 4 hours $SO_4^{2-}$ simulation.*

| Pos. [°2Θ] | FWHM Left [°2Θ] | Crystallite Size (nm) | Average Crystallite Size (nm) |
|---|---|---|---|
| 14.352 | 0.614 | 12.847 | 13.285 |
| 21.325 | 0.614 | 12.725 | |
| 27.092 | 0.409 | 18.884 | |
| 30.261 | 0.614 | 12.500 | |
| 33.478 | 0.409 | 18.602 | |
| 35.741 | 0.512 | 14.788 | |
| 36.436 | 0.512 | 14.759 | |
| 43.444 | 0.614 | 12.029 | |
| 46.979 | 0.512 | 14.250 | |
| 57.287 | 0.614 | 11.364 | |
| 60.614 | 0.819 | 8.384 | |
| 62.796 | 0.819 | 8.289 | |

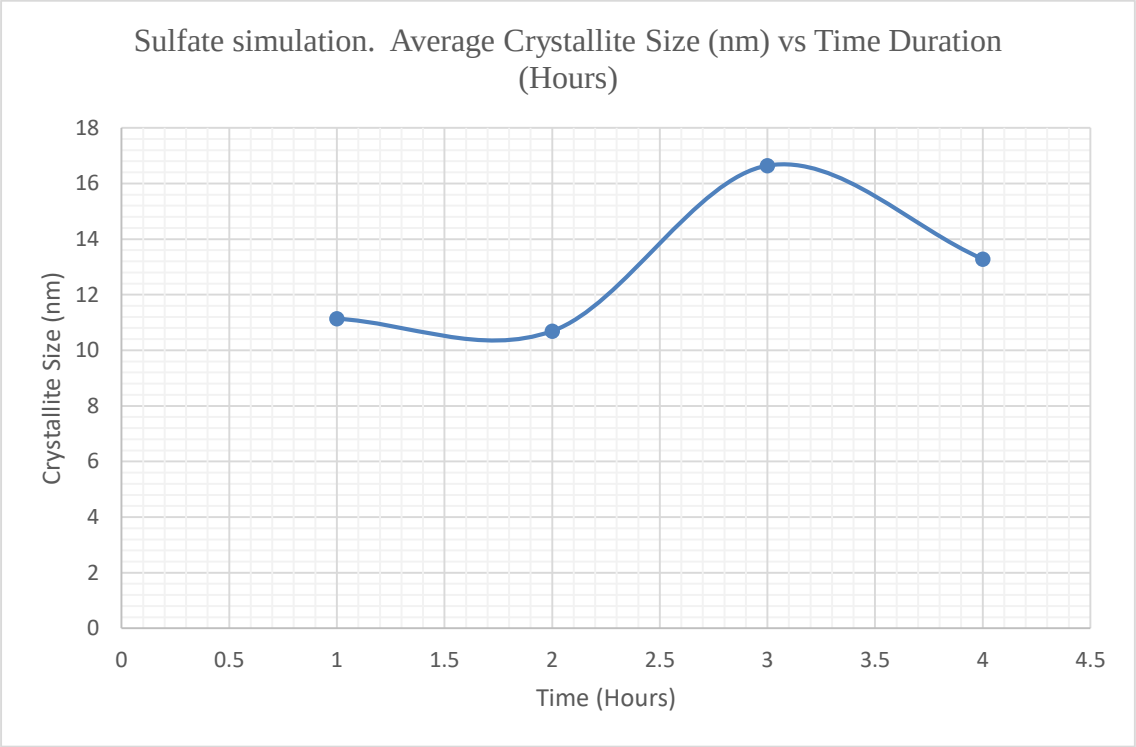


*Figure 3-15 Graph displaying average crystallite size (nm) vs time in hours. Sulfate simulation.*

The data for the sulfate simulation was calculated using Microsoft excel (see Tables 3-9 to 3-11). Average crystallite sizes for the sulfate simulations plotted against time in hours are at peak size at 3 hours (see Figure 3.14). The size gradually decreases beyond 3 hours.

# 4 DISCUSSIONS

A two-line ferrihydrite was synthesized using the solvent-deficient method which was confirmed through XRD measurements conducted on the sample. The ferrihydrite was the source of iron used in the simulation.

XRD results indicated the presence of siderite and magnetite for the $CO_3^{2-}$ and $SO_4^{2-}$ simulations respectively. Addition of Carbon to a simple Fe-O-H system introduces siderite, $FeCO_3$, within a pH range between 6.8 and 9.4, separating $Fe^{2+}$ from $Fe(OH)_2$. Goethite traces were found in association with siderite indicating oxidation. Magnetite was formed (Equation 4-1) unexpectedly in the $SO_4^{2-}$ simulations, while pyrite was not observed. The absence of pyrite could be attributed to the infinitesimal concentrations that could not be detected by the XRD. Formation of magnetite in sedimentary systems has been studied to involve various processes such as a) in-situ alteration during diagenesis b) fluid-mixing and related fluid/rock interactions c) microbial activity. Pyrite replacement by magnetite through surface dissolution/re-precipitation can be considered as an explanation (Brothers et al., 1996).

$$2Fe^{3+} + Fe^{2+} + 8OH^- \rightarrow Fe_3O_4 + 4H_2O \qquad \text{(Equation. 4-1)}$$

Crystallite sizes calculated for the siderite and magnetite precipitates using Scherrer's equation indicated average sizes of 14.6286 nm and 12.9393 nm respectively. Compared to SEM images crystallite sizes 9 µm and 13 µm for magnetite and siderite respectively. The difference in sizes from the analytical measurements taken is quite notable and should be further investigated in future work. Chukanovite observed under SEM images as "platy-structured" minerals possibly formed through the following process (See Equations 4-2 and 4-3)

$$2Fe_{(s)} + 2H_2O_{(l)} \rightarrow 2Fe(OH)^+_{(aq)} + 2H^+ + 4e^- \ldots \text{(Equation. 4-2)}$$

$$2Fe(OH)^+_{(aq)} + CO_3^{2-}{}_{(aq)} \rightarrow Fe_2(OH)_2CO_3 \ldots \text{(Equation. 4-3)}$$

The PHREEQ program accurately predicted the formation of siderite upon running the carbonate simulation. Magnetite formation was contrary to the PHREEQ prediction of forming

pyrite on conducting the sulfate simulation. The formation of magnetite represents either partial reduction of ferrihydrite or the partial oxidation of an intermediate reduced phase. It might also be explainable through the highly alkaline nature of the sulfate solution, pH 13.4, as per the Eh-pH diagram.

$SO_4^{2-}$ mineral transformations can be described using the conceptual flow chart below (see Figure 4-1)

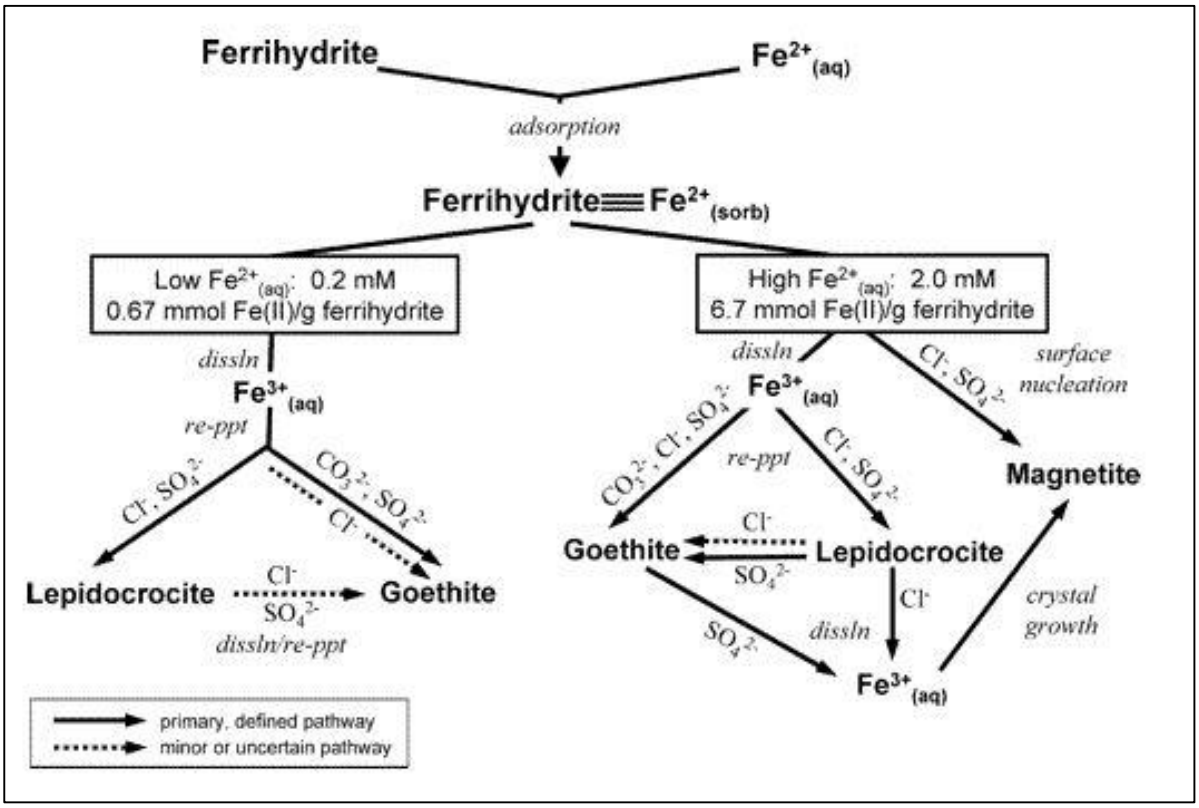


*Figure 4-1. $SO_4^{2-}$ mineral transformations involving Ferrihydrite (Hansel et al., 2005)*

# 5 CONCLUSIONS

The formation of siderite in all the carbonate simulations indicates its prevalence in the occurrence of the iron-carbonate minerals. This occurrence of siderite is contrary to its occurrence in nature, as it is not observed everywhere. The absence of pyrite from the $SO_4^{2-}$ and $S^{2-}$ simulations was unclear and the formation of magnetite could have been an indication of transformation through processes such as re-precipitation or dissolution. The ease of precipitating siderite during the carbonate simulations was an important aspect in sediments paleo magnetism, because siderite oxidation readily produces daughter magnetic minerals such as magnetite and hematite. This possibly explains the scarcity of siderite in nature. In conclusion, it is noted that siderite formed through $CO_3^{2-}$ simulation can transform to either goethite or chukanovite and the magnetite observed in the $SO_4^{2-}$ simulation could have possibly formed due to pyrite transformation or re-precipitation.

Future works should include conducting similar experiments with varying $CO_3^{2-}$, $SO_4^{2-}$ and $S^{2-}$ solution concentrations.

## REFERENCES

Altun, N. E., Güler, T., & Akdemir, Ü. (2010, October). Pyrite flotation–a review. In *Proceedings of the XIIth International Mineral Processing Conference, Cappadochia-Nevşehir, Turkey* (pp. 295-303).

Berner, D. (n.d.). Chukanovite. Retrieved from http://webmineral.com/specimens/picshow.php?id=3461&target=Chukanovite#.XgG6A-hKg4m.

Berner, R. A. (1981). A new geochemical classification of sedimentary environments. *Journal of Sedimentary Research*, *51*(2), 359-365.

Berner, R. A. (1984). Sedimentary pyrite formation: an update. *Geochimica et cosmochimica Acta*, *48*(4), 605-615.

Bennington, B. (1999, October). Retrieved December 20, 2019, from https://peopleold.hofstra.edu/J_B_Bennington/135notes/diagenesis.html.

Boomer, I., Aladin, N., Plotnikov, I., & Whatley, R. (2000). The palaeolimnology of the Aral Sea: a review. *Quaternary Science Reviews*, *19*(13), 1259-1278.

Boomer, I. (1993). Paleoenvironmental indicators from Late Holocene and contemporary ostracoda of the Aral Sea. *Paleogeography, Paleoclimatology, Paleoecology*, *103*(3-4), 141-153.

Brookins, D. G. (2012). *Eh-pH diagrams for geochemistry*. Springer Science & Business Media.

Brothers, L. A., Engel, M. H., & Elmore, R. D. (1996). The late diagenetic conversion of pyrite to magnetite by organically complexed ferric iron. *Chemical Geology*, *130*(1-2), 1-14.

Campisano, C. J., Cohen, A. S., Arrowsmith, J. R., Asrat, A., Behrensmeyer, A. K., Brown, E. T., ... & Lamb, H. F. (2017). The Hominin Sites and Paleolakes Drilling Project: High-resolution paleoclimate records from the East African Rift System and their implications for understanding the environmental context of hominin evolution. *PaleoAnthropology*.

Cohen, A. S. (2003). *Paleolimnology: the history and evolution of lake systems*. Oxford University Press.

Davis, D. M., Deocampo, D., Rabideaux, N. M., & Campisano, C. J. (2017, December). a Mineralogical Analysis of Hspdp Core Samples from the Northern Awash Pliocene Hadar Formation, Ethiopia: the tale of an East African Paleolake. In *AGU Fall Meeting Abstracts*.

Deocampo, D.M. and Jones, B.F., (2014). Geochemistry of Saline Lakes. Treatise on Geochemistry 2nd Edition, Volume 7: Surface and Groundwater, Weathering and Soils (Drever, J.I., Ed.), p. 437-469

Drever, James I. (1997). The geochemistry of natural waters: surface and groundwater environments. Upper Saddle River, N.J.: Prentice Hall.

Fernandez, A., Tang, J., & Rosenheim, B. E. (2014). Siderite 'clumped' isotope thermometry: a new paleoclimate proxy for humid continental environments. *Geochimica et Cosmochimica Acta*, *126*, 411-421.

Hansel, C. M., Benner, S. G., & Fendorf, S. (2005). Competing Fe (II)-induced mineralization pathways of ferrihydrite. *Environmental Science & Technology*, *39*(18), 7147-7153.

Hlal, O. A. (2013). An integrated study of diagenesis and sequence stratigraphy in shore face sandstones; Ponta Grossa Formation (Devonian), Parana Basin, Brazil. Abstracts with Programs - Geological Society of America, 45(7), 124.

Jirsa, F., Gruber, M., Stojanovic, A., Omondi, S. O., Mader, D., Körner, W., & Schagerl, M. (2013). Major and trace element geochemistry of Lake Bogoria and Lake Nakuru, Kenya, during extreme draught. *Chemie der erde-geochemistry*, *73*(3), 275-282.

Lim, D. I., Jung, H. S., Yang, S. Y., & Yoo, H. S. (2004). Sequential growth of early diagenetic freshwater siderites in the Holocene coastal deposits, Korea. *Sedimentary Geology*, *169*(1-2), 107-120.

Micklin, P. (2010). The past, present, and future Aral Sea. *Lakes & Reservoirs: Research & Management*, *15*(3), 193-213.

Mozley, P. S. (1989). Relation between depositional environment and the elemental composition of early diagenetic siderite. *Geology*, *17*(8), 704-706.

Nodder, S. D., Boyd, P. W., Chiswell, S. M., Pinkerton, M. H., Bradford-Grieve, J. M., & Greig, M. J. (2005). Temporal coupling between surface and deep ocean biogeochemical processes in contrasting subtropical and subantarctic water masses, southwest Pacific Ocean. *Journal of Geophysical Research: Oceans*, *110*(C12)

Parkhurst, D. L., & Appelo, C. A. J. (1999). User's guide to PHREEQC (Version 2): A computer program for speciation, batch-reaction, one-dimensional transport, and inverse geochemical calculations. *Water-resources investigations report*, *99*(4259), 312.

Patterson, A. L. (1939). The Scherrer formula for X-ray particle size determination. *Physical review*, *56*(10), 978.

Phillips, W. R., & Griffen, D. T. (1981). *Optical mineralogy: the nonopaque minerals*. WH Freeman.

Pye, K., Dickson, J. A. D., Schiavon, N., Coleman, M. L., & Cox, M. (1990). Formation of siderite-Mg-calcite-iron sulphide concretions in intertidal marsh and sandflat sediments, north Norfolk, England. *Sedimentology*, *37*(2), 325-343.

Rodrigues, A. G., De Ros, L. F., Neumann, R., & Borghi, L. (2015). Paleoenvironmental implications of early diagenetic siderites of the Paraíba do Sul Deltaic Complex, eastern Brazil. *Sedimentary Geology*, *323*15-30. doi: 10.1016/j.sedgeo.2015.04.005

Russell, M. J., Hall, A. J., & Martin, W. (2010). Serpentinization as a source of energy at the origin of life. *Geobiology*, *8*(5), 355-371.

Schlüter, T. (1997). Geology of East Africa. Beiträge zur regionalen geologie der erde. In *Band* (Vol. 27). Gebrüder Borntraeger Berlin–Stuttgart.

Scoon, R. N. (2018). Lakes of the Gregory Rift Valley: Baringo, Bogoria, Nakuru, Elmenteita, Magadi, Manyara and Eyasi. In *Geology of National Parks of Central/Southern Kenya and Northern Tanzania* (pp. 167-180). Springer, Cham.

Smith, Stacey J, Page, Katharine, Kim, Hyunjeong, Campbell, Branton J, Boerio-Goates, Juliana, and Woodfield, Brian F. "Novel Synthesis and Structural Analysis of Ferrihydrite." Inorganic Chemistry. 51.11 (2012): 6421-424. Web.

Stucki, J. W., Golden, D. C., & Roth, C. B. (1984). Preparation and handling of dithionite-reduced smectite suspensions. *Clays and Clay Minerals*, *32*(3), 191-197.

Tarits, C., Renaut, R. W., Tiercelin, J. J., Le Hérissé, A., Cotten, J., & Cabon, J. Y. (2006). Geochemical evidence of hydrothermal recharge in Lake Baringo, central Kenya Rift Valley. *Hydrological Processes: An International Journal*, *20*(9), 2027-2055.

Trauth, M. H., Maslin, M. A., Deino, A. L., Strecker, M. R., Bergner, A. G., & Dühnforth, M. (2007). High-and low-latitude forcing of Plio-Pleistocene East African climate and human evolution. *Journal of Human Evolution*, *53*(5), 475-486.

Wood, J., & Guth, A. (2013). East Africa's Great Rift Valley: a complex rift system. *Geology. com*.

# APPENDIX A.

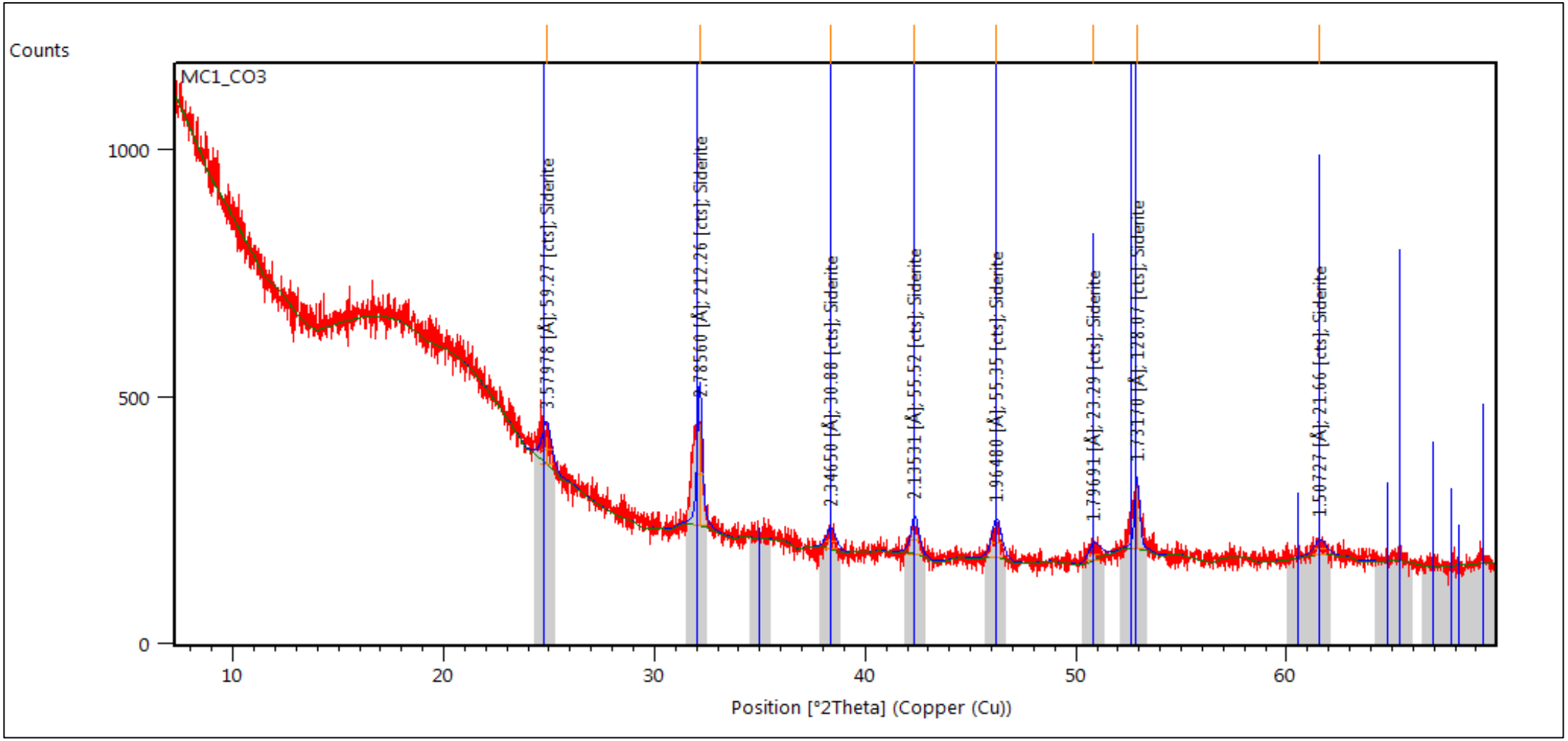
Counts
MC1_CO3
1000
500
0
3.57978 [Å]; 59.27 [cts]; Siderite
2.78560 [Å]; 212.26 [cts]; Siderite
2.34650 [Å]; 30.88 [cts]; Siderite
2.13531 [Å]; 55.52 [cts]; Siderite
1.96480 [Å]; 55.35 [cts]; Siderite
1.79691 [Å]; 23.29 [cts]; Siderite
1.73170 [Å]; 128.07 [cts]; Siderite
1.50727 [Å]; 21.66 [cts]; Siderite
10
20
30
40
50
60
Position [°2Theta] (Copper (Cu))

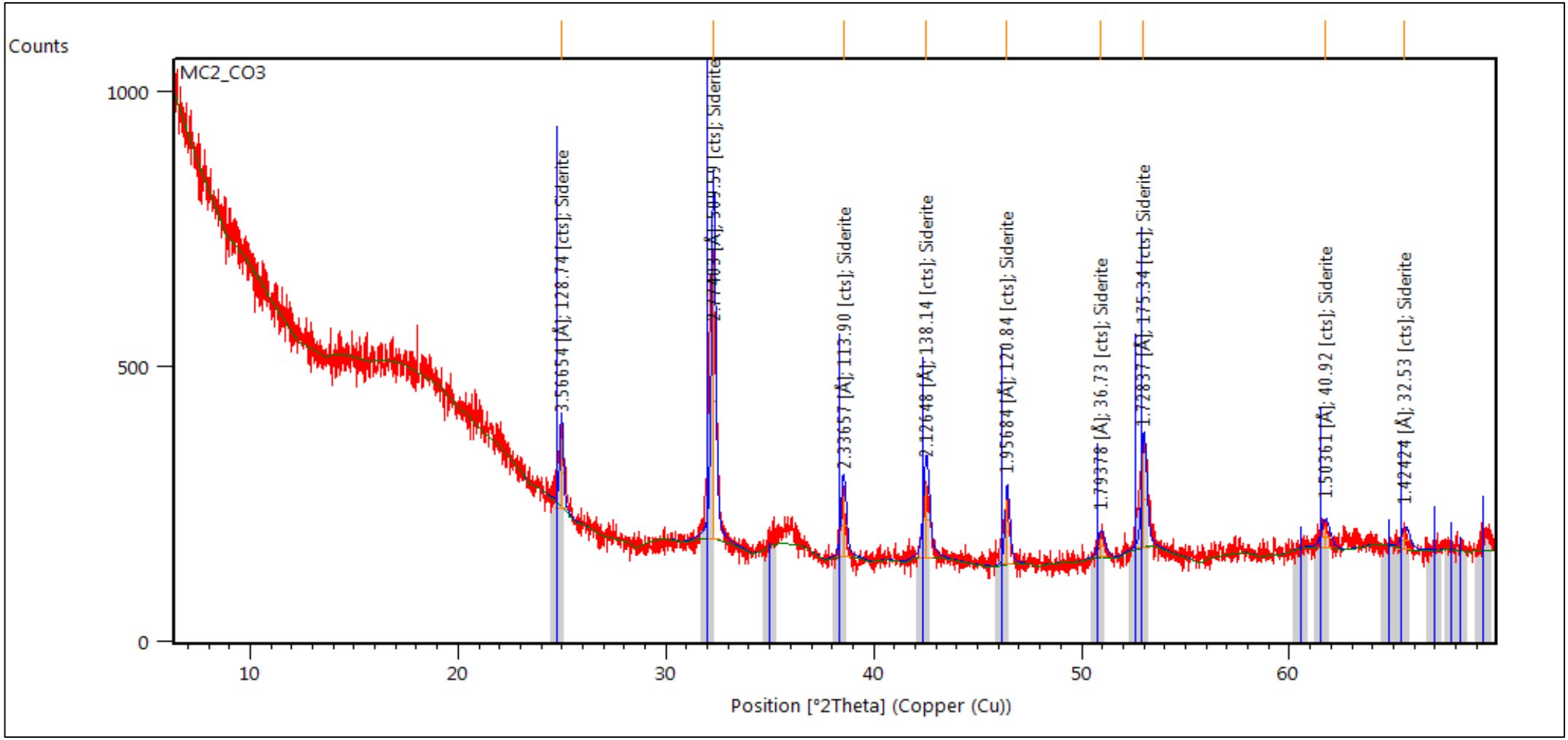
Counts
MC2_CO3
1000
500
0
3.56654 [Å]; 128.74 [cts]; Siderite
2.77403 [Å]; 309.59 [cts]; Siderite
2.33657 [Å]; 113.90 [cts]; Siderite
2.12648 [Å]; 138.14 [cts]; Siderite
1.95684 [Å]; 120.84 [cts]; Siderite
1.79378 [Å]; 36.73 [cts]; Siderite
1.72837 [Å]; 175.34 [cts]; Siderite
1.50361 [Å]; 40.92 [cts]; Siderite
1.42424 [Å]; 32.53 [cts]; Siderite
10
20
30
40
50
60
Position [°2Theta] (Copper (Cu))

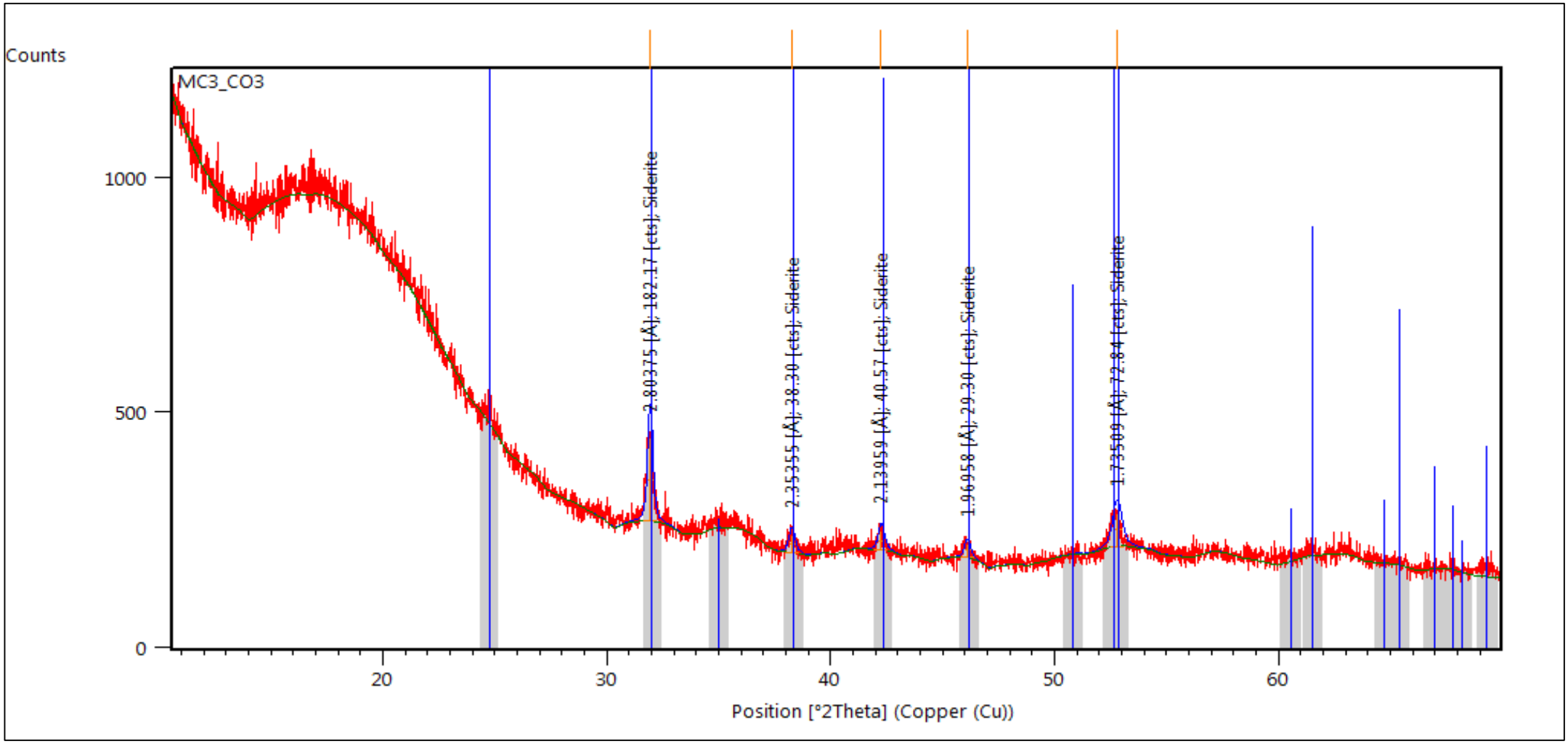
Counts
MC3_CO3
1000
500
0
2.80375 (Å); 182.17 (cts); Siderite
2.35355 (Å); 38.30 (cts); Siderite
2.13959 (Å); 40.57 (cts); Siderite
1.96958 (Å); 29.30 (cts); Siderite
1.73509 (Å); 72.84 (cts); Siderite
20
30
40
50
60
Position [°2Theta] (Copper (Cu))

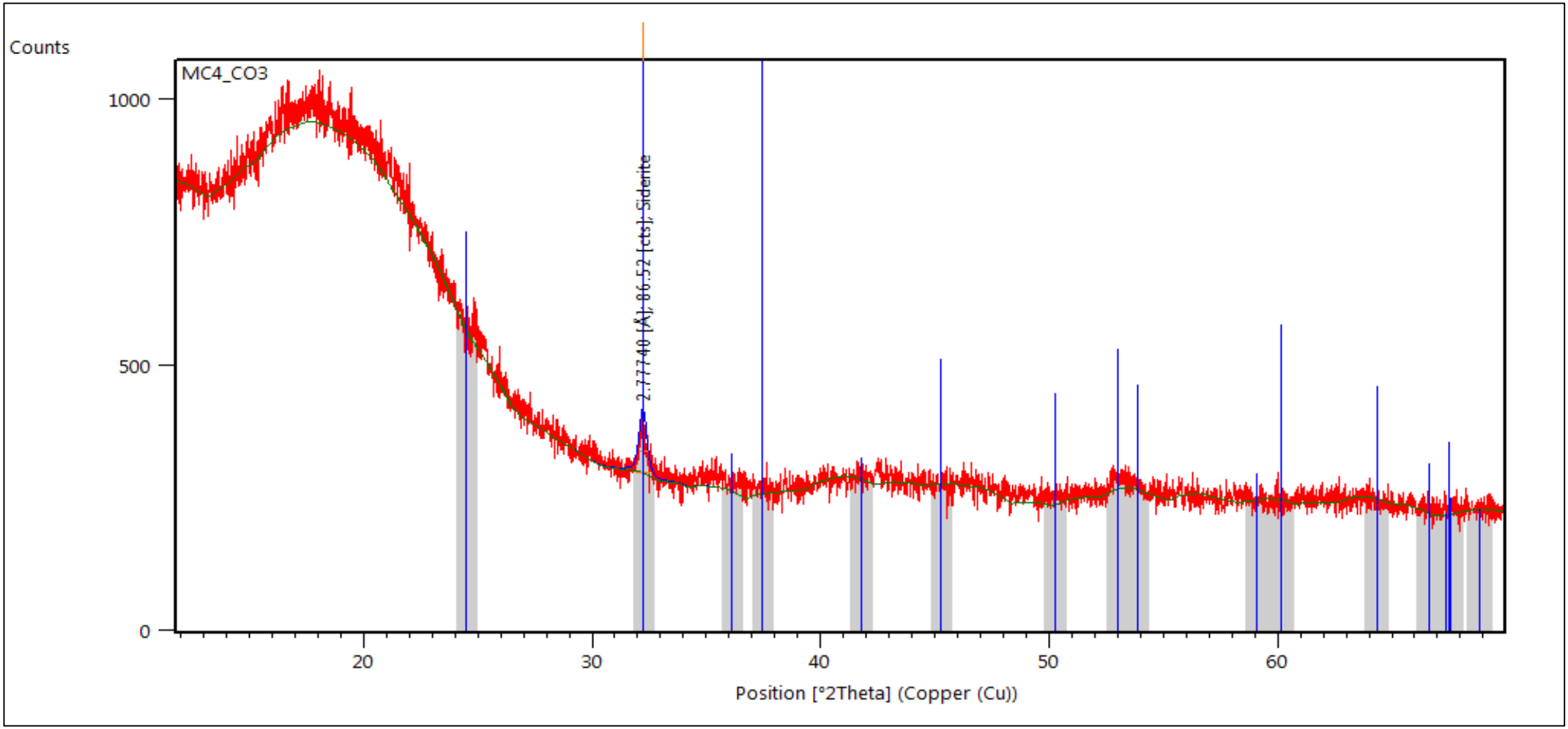
Counts
MC4_CO3
1000
500
0
2.77740 [Å], 86.52 [cts], Siderite
20
30
40
50
60
Position [°2Theta] (Copper (Cu))

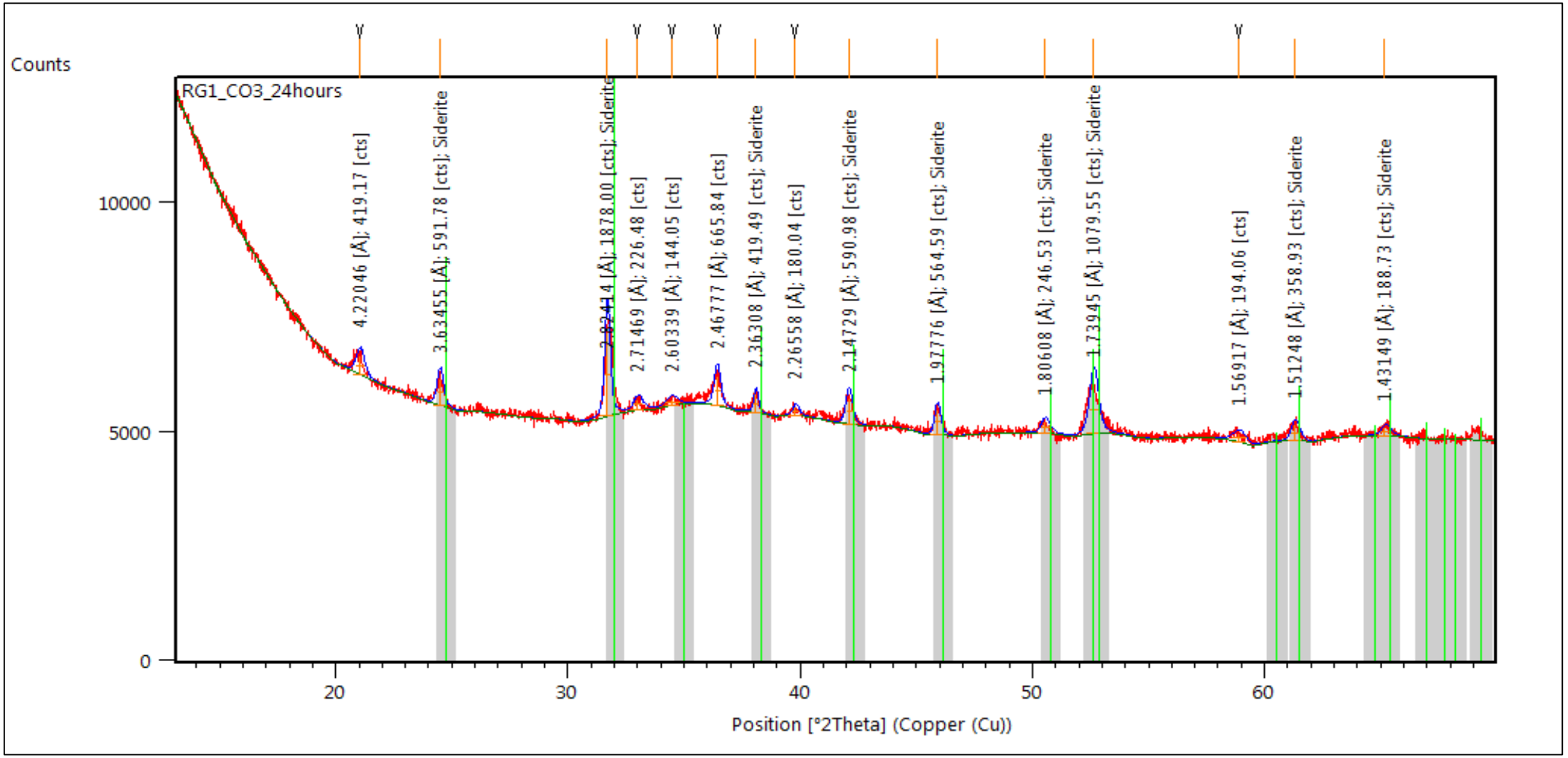
Counts
RG1_CO3_24hours
10000
5000
0
20
30
40
50
60
Position [°2Theta] (Copper (Cu))
4.22046 [Å]; 419.17 [cts]
3.63455 [Å]; 591.78 [cts]; Siderite
2.71469 [Å]; 226.48 [cts]
2.60339 [Å]; 144.05 [cts]
2.46777 [Å]; 665.84 [cts]
2.36308 [Å]; 419.49 [cts]; Siderite
2.26558 [Å]; 180.04 [cts]
2.14729 [Å]; 590.98 [cts]; Siderite
1.97776 [Å]; 564.59 [cts]; Siderite
1.80608 [Å]; 246.53 [cts]; Siderite
1.73945 [Å]; 1079.55 [cts]; Siderite
1.56917 [Å]; 194.06 [cts]
1.51248 [Å]; 358.93 [cts]; Siderite
1.43149 [Å]; 188.73 [cts]; Siderite

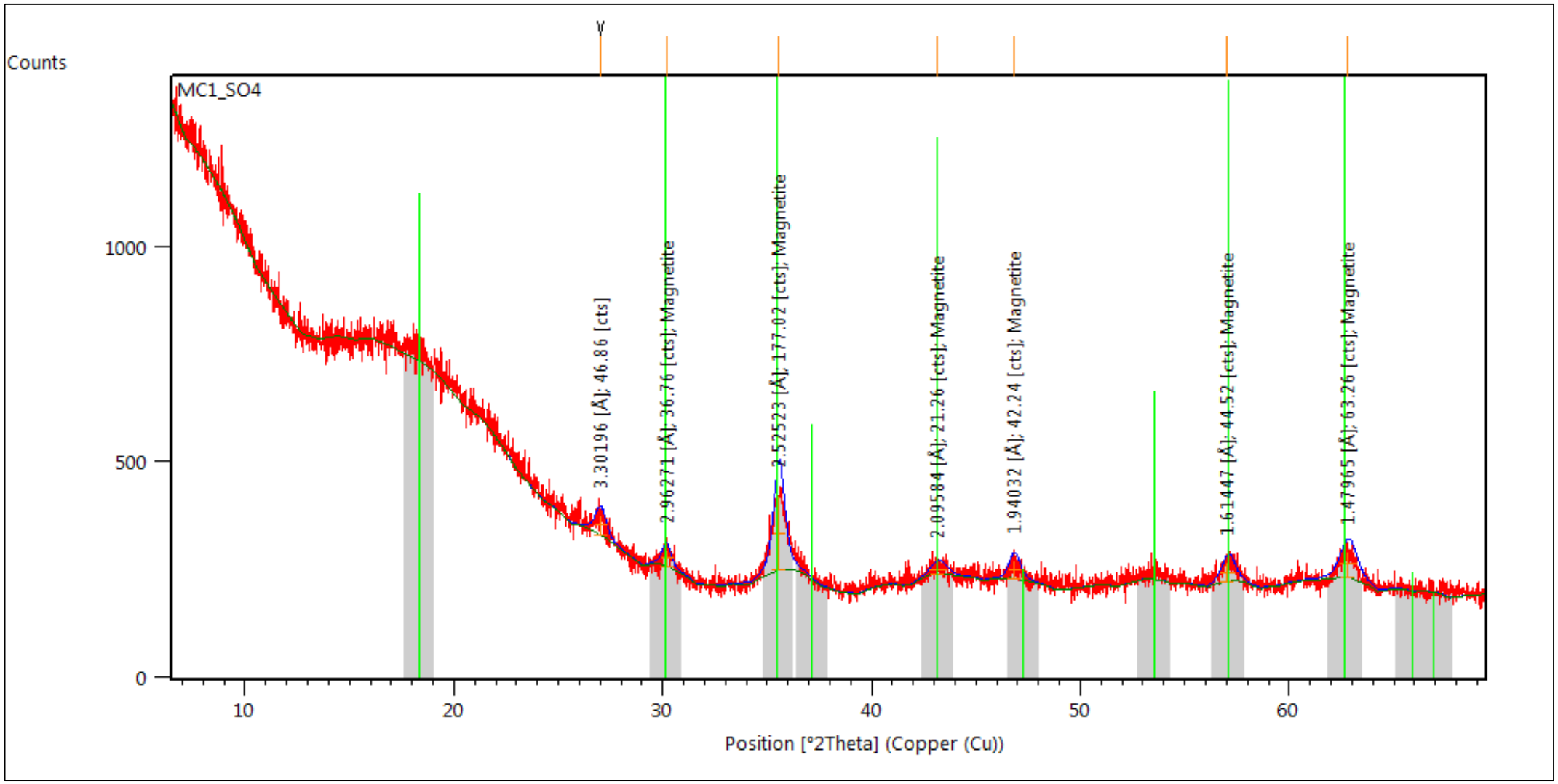
Counts
MC1_SO4
1000
500
0
10
20
30
40
50
60
Position [°2Theta] (Copper (Cu))
3.30196 [Å]; 46.86 [cts]
2.96271 [Å]; 36.76 [cts]; Magnetite
2.52523 [Å]; 177.02 [cts]; Magnetite
2.09584 [Å]; 21.26 [cts]; Magnetite
1.94032 [Å]; 42.24 [cts]; Magnetite
1.61447 [Å]; 44.52 [cts]; Magnetite
1.47965 [Å]; 63.26 [cts]; Magnetite

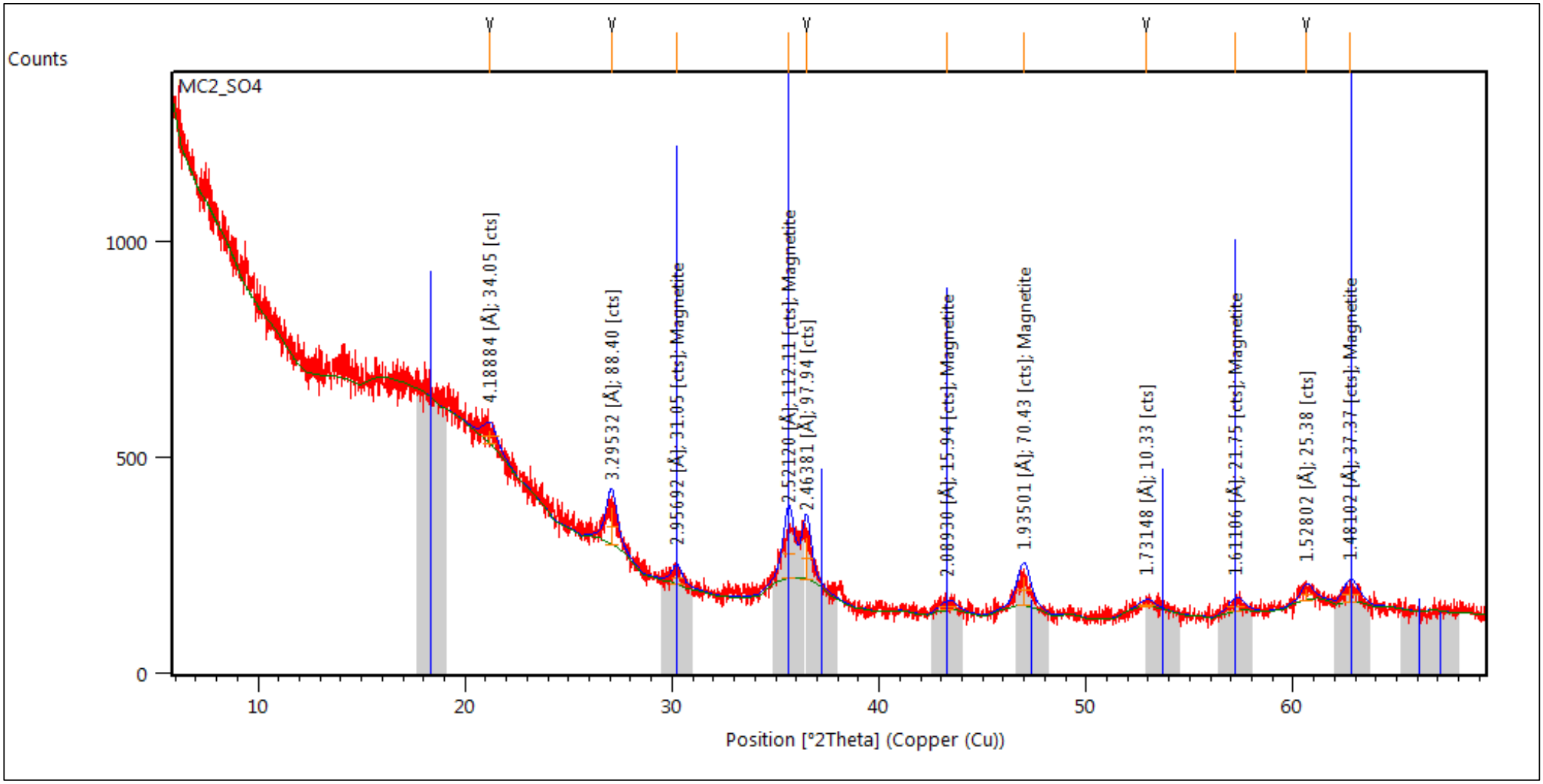
Counts
MC2_SO4
1000
500
0
4.18884 [Å]; 34.05 [cts]
3.29532 [Å]; 88.40 [cts]
2.95692 [Å]; 31.05 [cts]; Magnetite
2.52120 [Å]; 112.11 [cts]; Magnetite
2.46381 [Å]; 97.94 [cts]
2.08930 [Å]; 15.94 [cts]; Magnetite
1.93501 [Å]; 70.43 [cts]; Magnetite
1.73148 [Å]; 10.33 [cts]
1.61106 [Å]; 21.75 [cts]; Magnetite
1.52802 [Å]; 25.38 [cts]
1.48102 [Å]; 37.37 [cts]; Magnetite
10
20
30
40
50
60
Position [°2Theta] (Copper (Cu))

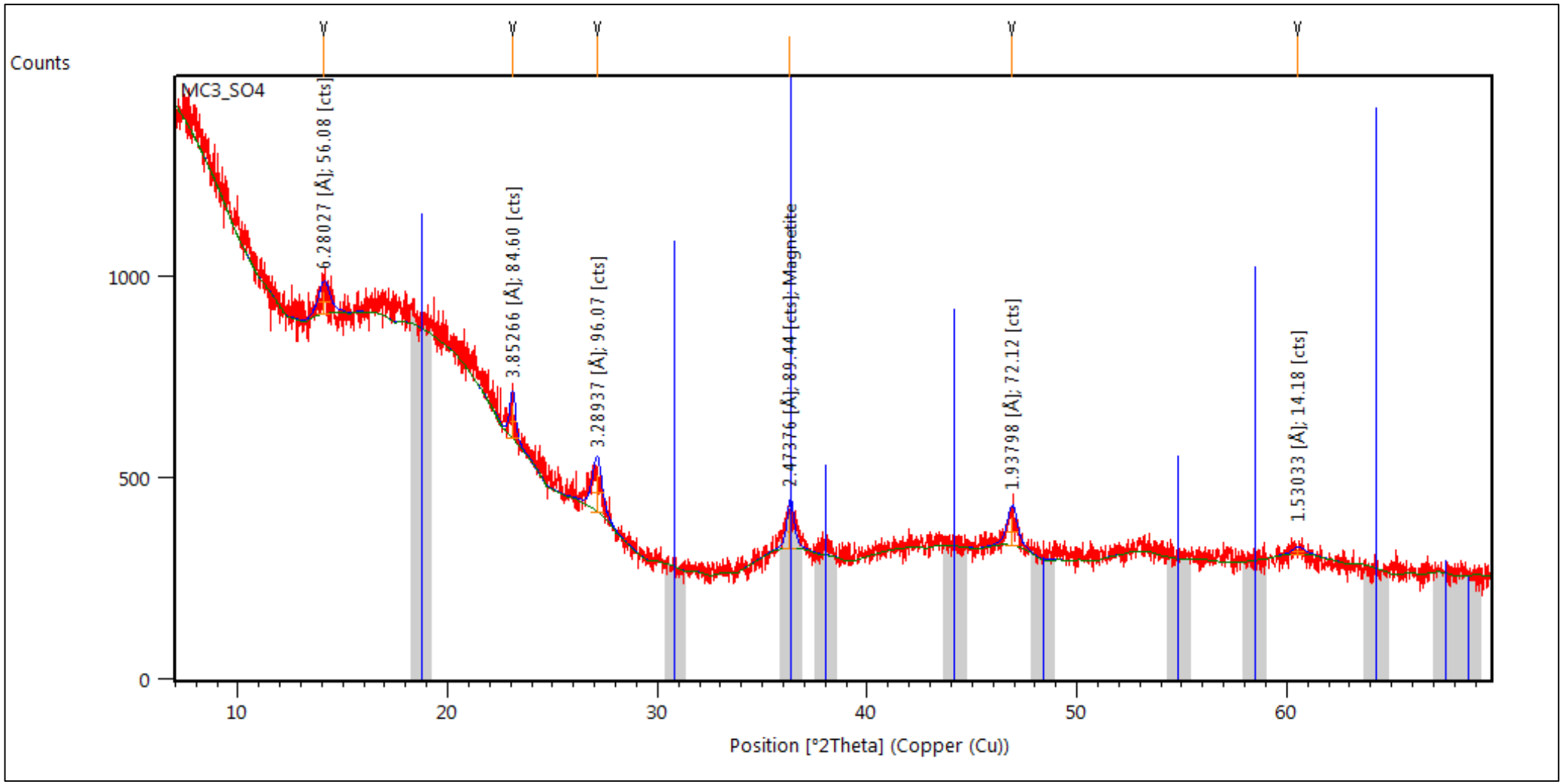
Counts
MC3_SO4
6.28027 [Å]; 56.08 [cts]
3.85266 [Å]; 84.60 [cts]
3.28937 [Å]; 96.07 [cts]
2.47376 [Å]; 89.44 [cts]; Magnetite
1.93798 [Å]; 72.12 [cts]
1.53033 [Å]; 14.18 [cts]
1000
500
0
10
20
30
40
50
60
Position [°2Theta] (Copper (Cu))

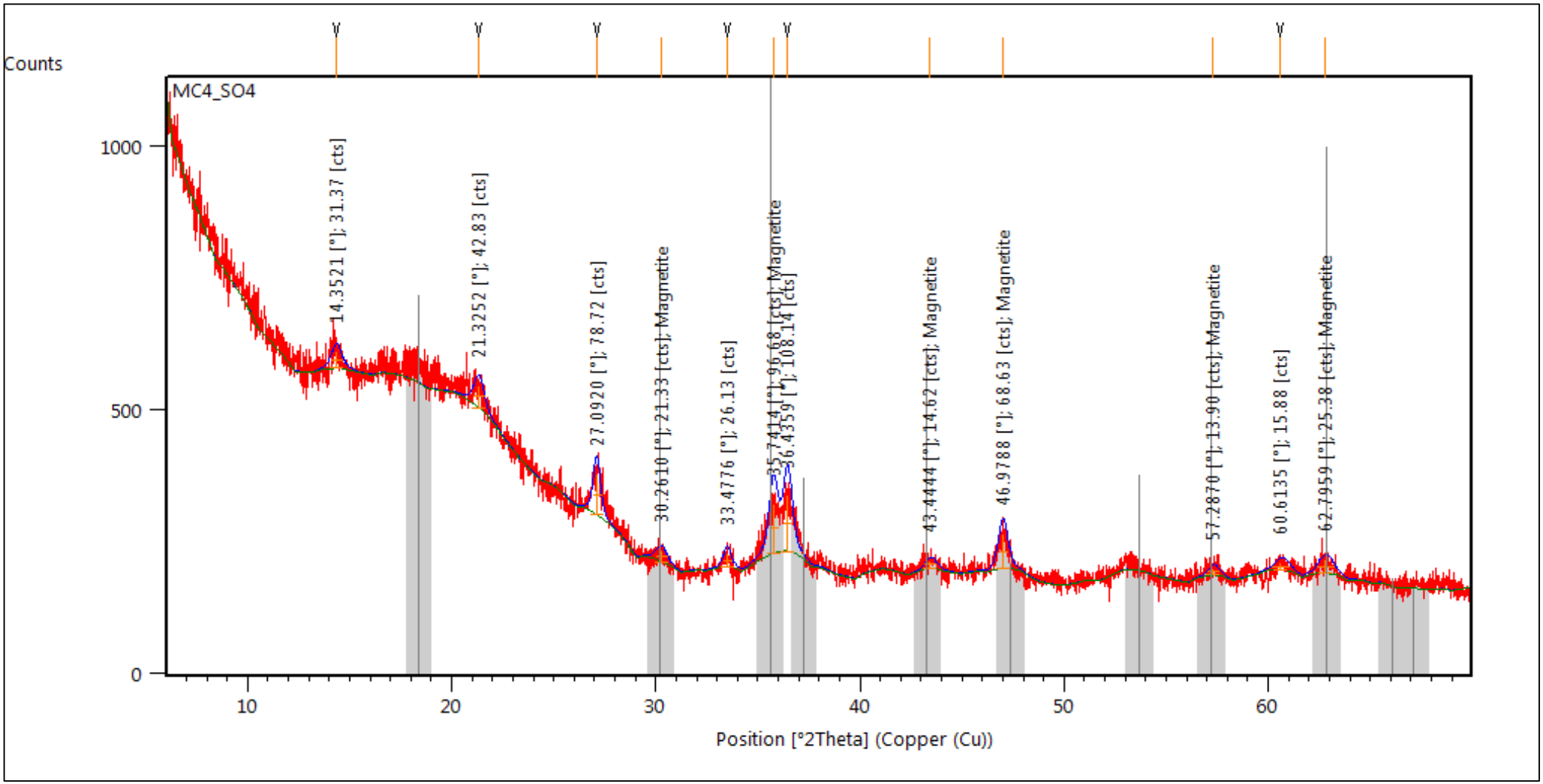
Counts
MC4_SO4
1000
500
0
14.3521 [°]; 31.37 [cts]
21.3252 [°]; 42.83 [cts]
27.0920 [°]; 78.72 [cts]
30.2610 [°]; 21.33 [cts]; Magnetite
33.4776 [°]; 26.13 [cts]
35.7414 [°]; 96.68 [cts]; Magnetite
36.4359 [°]; 108.14 [cts]
43.4444 [°]; 14.62 [cts]; Magnetite
46.9788 [°]; 68.63 [cts]; Magnetite
57.2870 [°]; 13.90 [cts]; Magnetite
60.6135 [°]; 15.88 [cts]
62.7959 [°]; 25.38 [cts]; Magnetite
10
20
30
40
50
60
Position [°2Theta] (Copper (Cu))

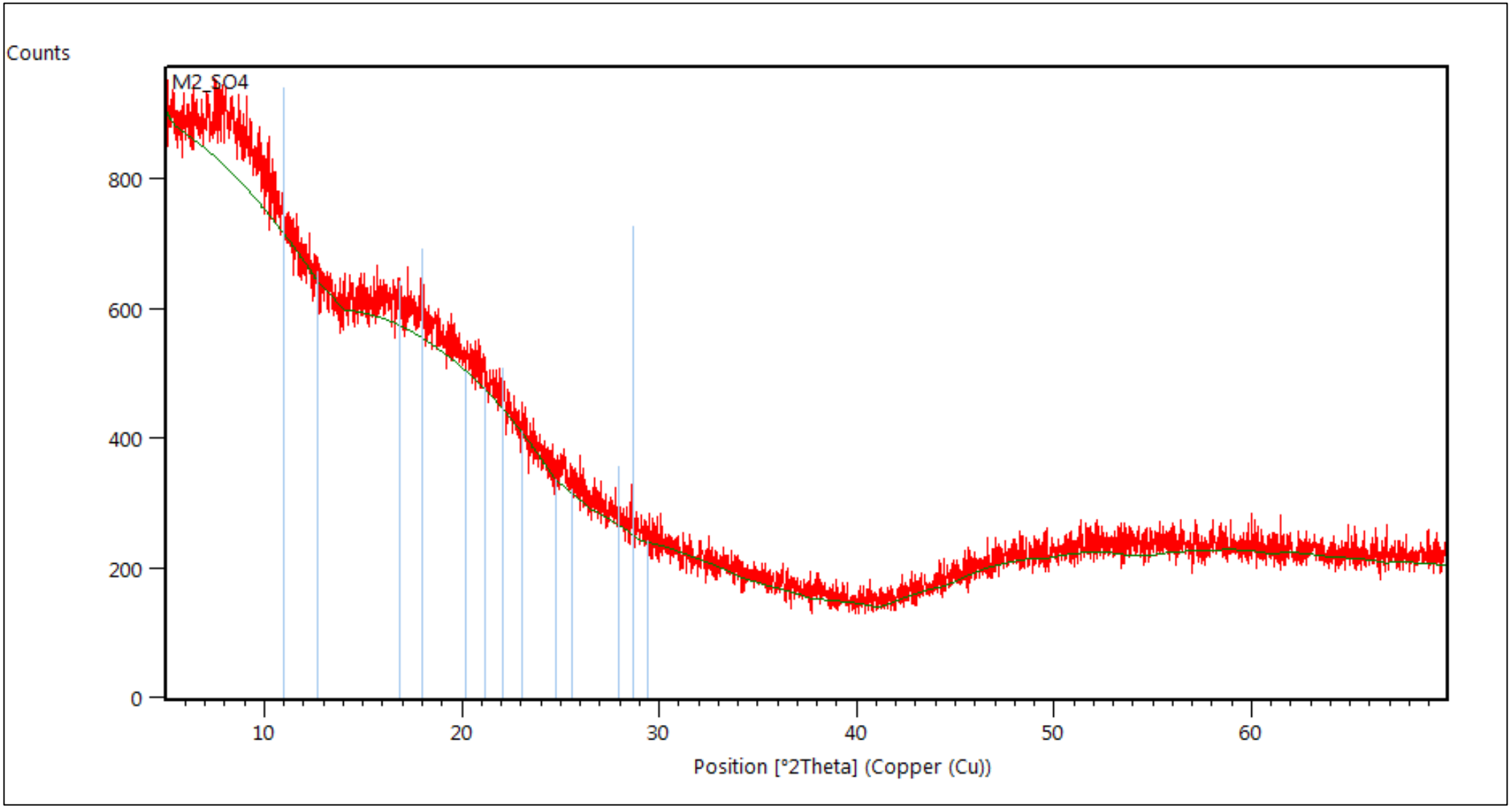
Counts
M2_SO4
800
600
400
200
0
10
20
30
40
50
60
Position [°2Theta] (Copper (Cu))

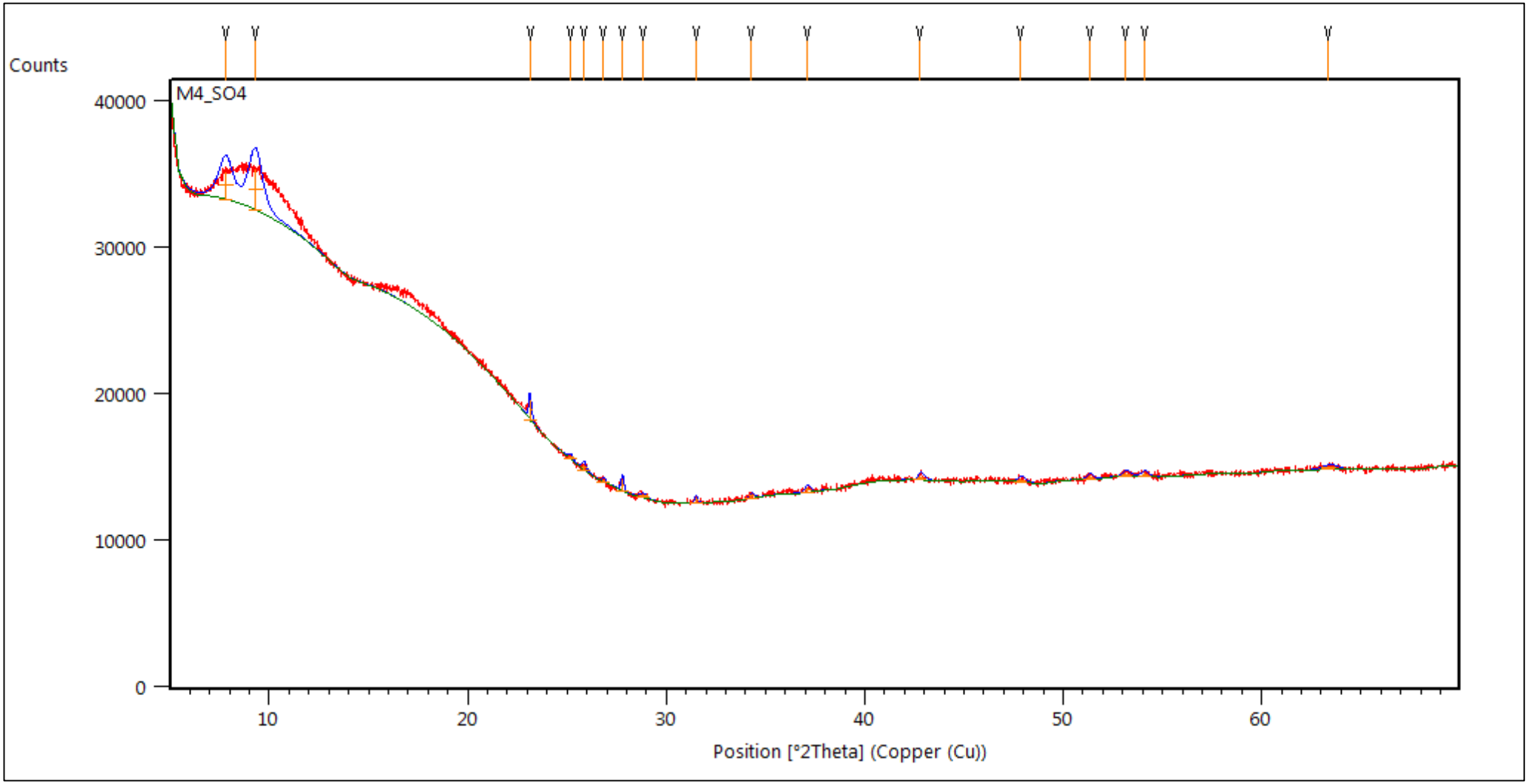
Counts
M4_SO4
40000
30000
20000
10000
0
10
20
30
40
50
60
Position [°2Theta] (Copper (Cu))